

Photonic-band-gap architectures for long-lifetime room-temperature polariton condensation in GaAs quantum wells

Jian-Hua Jiang,^{1,2} Pranai Vasudev,¹ and Sajeer John^{1,2,*}

¹*Department of Physics, University of Toronto, Toronto, Canada, Ontario M5S 1A7*

²*College of Physics, Optoelectronics, and Energy and Collaborative Innovation Center of Suzhou Nano Science and Technology, Soochow University, 1 Shizi Street, Suzhou 215006, China*

(Received 6 June 2017; published 12 October 2017)

We describe AlGaAs photonic-crystal architectures that simultaneously realize strong exciton-photon coupling, long polariton lifetime, and room-temperature polariton Bose-Einstein condensation (BEC). Strong light trapping, induced by a 3D photonic band gap (PBG), leads to peak field intensity 20 times as large as that in an AlGaAs Fabry-Pérot microcavity and exciton-photon coupling as large as 20 meV (i.e., vacuum Rabi splitting 40 meV). The strong exciton-photon coupling, small polariton effective mass, and long polariton lifetime lead to possible realizations of *equilibrium* room-temperature BEC. We also consider the influence of polarization degeneracy and symmetry breaking in the ground state on the BEC-onset temperature and condensate fraction. Woodpile and slanted-pore PBG structures that break X-Y symmetry facilitate larger condensate fractions at moderate temperatures. The effects of electronic and photonic disorder are marginal, thanks to the 3D photonic band gap.

DOI: [10.1103/PhysRevA.96.043827](https://doi.org/10.1103/PhysRevA.96.043827)

I. INTRODUCTION

Bose-Einstein condensation [1] (BEC) is a remarkable state of many-body quantum coherence. Besides the celebrated observation of BEC in liquid helium [2,3], superconductors [4,5], and ultracold atomic gases [6,7], BEC has also been realized in exciton-polariton systems in semiconductor microcavities during the last decade [8–12]. Polaritons are quasiparticles composed of photon and exciton and inherit their special properties. Polaritonic BEC can be realized in much simpler and lower-cost systems at much higher temperatures [13,14], compared to the ultralow-temperature and ultrahigh-vacuum required for atomic BEC. In addition, thanks to the “half-photon” nature of polaritons [15], quasiparticle and statistical properties of the condensate can be directly monitored through polariton luminescence. This special property has been exploited, together with quantum optical methods, to measure the spatially resolved phase coherence and to identify 2π phase rotations of a quantized vortex [16,17]. The research field of polariton BEC has been advanced through developments of materials and growth technologies, techniques for manipulating and measuring polariton coherence, which facilitate progress in fundamental physics and applications [18–21]. Proposals of using polariton BEC as building blocks for quantum simulation and computation have also been raised [22]. Electrically pumped polariton lasing [23] and polariton all-optical switches [24] and transistors [25] have been realized in recent experiments.

Existing realizations of polariton BEC suffer from short polariton lifetimes, ranging from approximately 1 ps to 100 ps [13,19] in Fabry-Pérot (FP) microcavities. This short lifetime prevents the polariton condensate from reaching a full thermal equilibrium with the host lattice, though there are also claims of fully thermalized condensates in these one-dimensional geometries [26]. Recently, there have been debates on the nature of the observed polariton BEC, whether it is a quasiequilibrium

(thermodynamic) state or a nonequilibrium (kinetically driven) state [13,27]. In this work, we use quasiequilibrium to refer to the fact that the polariton gas may thermalize with itself (however, not with the host lattice) due to polariton-polariton scattering and its energy distribution may be fitted by a Bose-Einstein distribution with a higher effective temperature than that of the lattice [28,29]. The origin of the short lifetime is due to the coupling of excitons to leaky off-normal photonic modes. In Fabry-Pérot microcavities, there is a one-dimensional photonic stop gap and the $k = 0$ normal photonic mode can be made to arbitrarily high quality (as high as 3×10^5 [26]). However, for off-normal propagation, there is no photonic band gap [30], since there is no periodic modulation in the dielectric constant to coherently scatter light. This results in weakly confined modes which can couple easily to vacuum modes outside the cavity. In this work, we refer to these off-normal propagating modes in Fabry-Pérot cavities as leaky modes. Several works [10,12,19] claim that the polariton Bose condensates in microcavities occur due to the strong coupling between an excitonic mode and this high quality, $k = 0$ normal photonic mode. However, this would be forbidden in two dimensions, as a Bose condensate with zero momentum would be infinitely spatially extended, which is forbidden by the Mermin-Wagner theorem. Therefore, in Fabry-Pérot microcavities, the Bose-Einstein condensates resulting from the coupling of an exciton to an off-normal, lower quality $k \neq 0$ leaky mode tend to have small lifetimes, on the order of a few ps. For this reason, the problem of short polariton lifetime cannot be overcome by various proposals involving higher quality cavities [18,19,28,31–33]. Due to the lack of a full three-dimensional photonic band gap, this problem is intrinsic to the Fabry-Pérot microcavities. There may exist other types of phase transitions, such as the Berezinskii-Kosterlitz-Thouless phase transition involving the appearance of topological defects such as quantized vortices, that may occur for polaritons in two-dimensional systems. Several works in the literature, for example Refs. [16,17,21,34,35], associate polariton condensates with this transition. In our work, we use the word condensate to refer exclusively to Bose-Einstein condensation.

*john@physics.utoronto.ca

In this work we utilize a 3D photonic band gap (PBG) to suppress polariton radiative decay [28,31,32,36]. The existence of a 3D PBG makes the structure robust against disorder which is unavoidable in fabrication processes and eliminates leaky modes, even in off-normal directions. Therefore, in a 3D PBG architecture, we can be assured that the exciton couples only to a strongly confined, nonleaky photonic mode. Experimentally, photonic-crystal (PhC) microcavities with a quality factor over 10^6 and photonic lifetime of 2 ns have been reported in Ref. [37]. If polariton spontaneous emission is suppressed by the PBG [38], then polariton decay is limited by nonradiative exciton recombination processes which are usually much slower for semiconductors with medium or large band gap at low and moderate carrier densities. Experimental measurements reveal that the photoluminescence decay in GaAs quantum wells (QW) at room temperature is about 250 ps [39]. This sets the lower bound of the polariton lifetime in a 3D PBG material. Such a time scale is already sufficient for the establishment of thermal equilibrium of polariton gases at room temperature in GaAs QWs where energy relaxation due to longitudinal-optical phonon scattering is very efficient (scattering time ~ 0.2 ps as deduced from exciton homogeneous linewidth) [40].

In this work, we further develop our road map for room-temperature thermal equilibrium polariton BEC in photonic-crystal architectures. Previously, we suggested room-temperature equilibrium polariton BEC is possible in InGaAs/InP quantum wells embedded in slanted-pore photonic crystals composed of InP [29]. Compared to GaAs quantum wells with an exciton binding energy of 10 meV, the exciton binding energy in InGaAs QWs is only 7 meV. This makes the formation of the exciton-polaritons at room temperature in InGaAs more challenging (polariton formation is needed to stabilize the exciton). Compared to the exciton recombination energy of approximately 1966 meV in GaAs QWs, the value for InGaAs QWs is only 944 meV. (Here, InGaAs refers to $\text{In}_{0.53}\text{Ga}_{0.47}\text{As}$ and the wells are 3 nm in width, surrounded by 7 nm InP barriers. The band gap of InGaAs depends on the Ga fraction and can range from 0.354 eV to 1.4 eV [29].) This increased exciton recombination energy in GaAs induces larger light-matter coupling strengths. Finally, the dielectric constant of the cladding PBG material differs between the two systems. For AlGaAs (in the case of GaAs QWs), $\epsilon = 9.54$, while for InP (in the case of InGaAs QWs), $\epsilon = 10.4$. Overall, there is weaker exciton-photon coupling and weaker light localization in the InGaAs system relative to the GaAs system. This weaker light-matter coupling strength results in more photonlike (than in GaAs-based systems) polaritons, assuming a fixed exciton-photon detuning. In turn, this allows for larger polariton densities to be considered, since the polariton density is constrained only in that the effective exciton density (in any one QW) cannot exceed the excitonic saturation density. These larger available densities provide a specific route to room-temperature BEC in the InGaAs-based system. The strategy for achieving high-temperature BEC in our GaAs-based system is somewhat different. The larger exciton-photon coupling strength in GaAs leads to more excitonlike polaritons. As a result of the larger photonic band gap (~ 100 meV in GaAs systems compared to ~ 50 meV in InGaAs systems), the alternative strategy for GaAs is

to consider larger detunings and produce more photonlike polaritons that favor room-temperature BEC. Together, our studies of InGaAs and GaAs suggest two methodologies for realizing room-temperature BEC: either increasing the polariton density or increasing the exciton-photon detuning.

In our GaAs quantum well system, we use AlGaAs-based woodpile and slanted-pore PhC microcavities to enhance polariton lifetime as well as to achieve strong exciton-photon coupling up to about 20 meV [vacuum Rabi splitting (VRS) of 40 meV] which, together with an exciton-photon detuning of 40 meV, stabilizes polaritons and enables polariton BEC at and above room temperature. Structures similar to the woodpile photonic crystals proposed here have been fabricated in recent experimental works [41,42] where a range of tunability of the PhC cavity was demonstrated. The slanted-pore PhC can be fabricated by techniques such as ion beam lithography or direct laser writing [43–45]. In either case, a large 3D PBG allows a range of detuning between the exciton and the confined photonic bands that is important for engineering polariton composition, dispersion depths, and BEC.

This paper is organized as follows: In Sec. II we describe the structure of the confined photonic bands, excitons, and the polaritons in a symmetric woodpile PBG cavity. In Sec. III, we introduce a toy model polariton dispersion that emulates the results of detailed band structure calculations. In this toy model, we introduce X-Y symmetry breaking to lift the polarization degeneracy in the 2D polariton system and we delineate its effect on BEC and condensate fraction. The transition temperature for polariton BEC is studied in Sec. IV using realistic band structures for slanted-pore and asymmetric-woodpile PBG cavities. We discuss the effect of structural disorders in Sec. V and conclude in Sec. VI. Some of the details of the calculations are presented in the appendices. All results are based on combined calculations of the photonic band structures via the plane wave expansion method [46,47] and the electronic (excitonic) structure through the effective mass approximation (following the methods in Refs. [48] and [49]). The material parameters and the electronic band structure coefficients are taken from standard semiconductor handbooks [50,51] and compared with existing experimental data (see Appendices A, B, and C).

II. POLARITONS IN AlGaAs PHOTONIC CRYSTAL MICROCAVITIES

A. Cavity photons

The structure of our proposed (symmetric) woodpile microcavity is illustrated in Fig. 1(a). The slab in the middle breaks the lattice translation symmetry along the growth direction, whereas in the perpendicular plane such symmetry still remains. For this woodpile structure, the width and height of the x - and y -oriented rods are $0.25a$ and $0.3a$, respectively, where a is the in-plane lattice period. The woodpile crystals sandwiching the central slab are made of $\text{Al}_{0.8}\text{Ga}_{0.2}\text{As}$ with the refractive index taken as 3.1. The thickness of the central slab is $0.07a$. The lattice period a is tuned to engineer the photonic spectrum which is proportional to $1/a$. The thickness of the central slab is chosen to (i) accommodate a multiple-quantum well (MQW) system with two to three individual QWs and

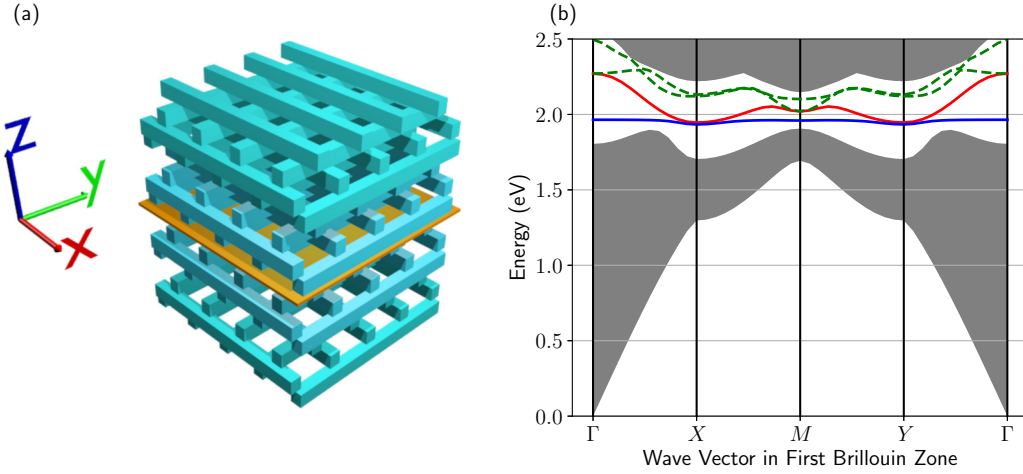


FIG. 1. AlGaAs PhC microcavity. Schematic of the woodpile. A central slab containing GaAs/AlGaAs QWs is sandwiched in the PhC. (b) Photonic band structure in the 2D Brillouin zone for the structure depicted in (a). The gray (shaded) regions represent the bulk photonic bands. The red (solid) curve in the band gap denotes the lowest confined photonic band. It is placed close to the QW exciton emission line and contributes significantly to the lower polariton branch (the blue [solid] curve below the lowest confined photonic band). Other confined photonic bands (represented by the green [dashed] curves) contribute much less to the formation of the lower polariton branch. The enlarged figures with focus on the band gap region are shown in Fig. 2. In obtaining these curves, the exciton-photon detuning at the X point is $\Delta_{\vec{Q}^{(x)}} = 20$ meV for a lattice constant of $a = 267$ nm. The light-matter coupling strength, taken at the X point, between an exciton (not shown) and the lowest guided photonic mode is $\hbar\Omega_{\vec{Q}^{(x)}} = 20$ meV, for three 2 nm GaAs QWs with 4 nm AlGaAs barriers in the central slab.

(ii) maintain a remaining band gap (gap-to-midgap ratio) of $\gtrsim 5\%$ between the lowest 2D guided band and the lower 3D band edge and prevent the radiative decay of the excitons. The QWs are made of GaAs, while the barriers between QWs are made of AlAs. The dielectric constant of the MQWs is taken approximately as the average value of the dielectric constants of GaAs and AlAs. The central slab with MQWs is where the photonic fields are confined. The strong light trapping induced by the 3D PBG enables strong coupling between the QW excitons and photons. The structure in Fig. 1(a) is optimized for strong exciton-photon coupling, as revealed by the distribution of the photonic field (see Appendix D). Related structures have been fabricated by Ogawa *et al.* [41,42]. The photonic-band-structure calculation for the structure shown in Fig. 1(a) via the plane wave expansion method yields a PBG to central frequency ratio of 12%, with several confined photonic bands in the gap [see Fig. 1(b)]; for details, see Appendix A. When the exciton recombination energy is close to the lowest confined photonic band, this band dominates the properties of the lower polariton branch [31–33]. There are two degenerate minima in the energy spectrum, located at $\vec{Q}^{(x)} = (\frac{\pi}{a}, 0)$ and $\vec{Q}^{(y)} = (0, \frac{\pi}{a})$, respectively. Around those energy minima the dispersion is approximately parabolic as

$$\hbar\omega_{\vec{q}} = \hbar\omega_0^{(v)} + \frac{\hbar^2(q_x - Q_x^{(v)})^2}{2m_x^{(v)}} + \frac{\hbar^2(q_y - Q_y^{(v)})^2}{2m_y^{(v)}}, \quad (1)$$

with $v = x, y$. The symmetric-woodpile structure possesses a D_{2d} symmetry with two mirror planes, the y - z and x - z planes [52], if there are an equal number of layers of rods above and below the slab [cf. Fig. 1(a)]. This symmetry ensures a C_{4v} symmetry for the dispersion of the lowest 2D confined photonic band in the 2D \vec{q} space (i.e., the q_x - q_y plane), which dictates $m_x^{(x)} = m_y^{(y)}$, $m_x^{(y)} = m_y^{(x)}$, $\omega_0^{(x)} = \omega_0^{(y)}$.

If $a = 300$ nm, the effective masses are $m_x^{(x)} = 7.1 \times 10^{-6} m_0$ and $m_y^{(y)} = 1.4 \times 10^{-5} m_0$ at the $\vec{Q}^{(x)}$ point in the woodpile structure, with m_0 being the bare electron mass in vacuum. The density of states mass is $m_{dos} = \sqrt{m_x^{(x)} m_y^{(y)}} = 1.0 \times 10^{-5} m_0$ when $a = 300$ nm. Since Maxwell's equations are scale invariant, the above dispersion is invariant under the continuous scaling transformation $a \rightarrow a/s$, $\omega \rightarrow s\omega$, and $q \rightarrow sq$, which reveals that ω_0 , $m_x^{(v)}$, and $m_y^{(v)}$ are proportional to $1/a$.

The electric field of a single cavity-confined photon in the i^{th} band with wave vector \vec{q} is (in SI units)

$$\vec{E}_{i,\vec{q}}(\vec{r}) = \sqrt{\frac{\hbar\omega_{i,\vec{q}}}{2\varepsilon_0 S}} \vec{u}_{i,\vec{q}}(\vec{r}) e^{i\vec{q}\cdot\vec{\rho}}. \quad (2)$$

Here ε_0 is the vacuum permittivity, S is the area of the structure in the x - y plane. $\vec{r} = (\vec{\rho}, z)$ with $\vec{\rho} = (x, y)$ being the coordinate vector in the x - y plane. $\omega_{i,\vec{q}}$ is the frequency of the photon. In PhC microcavities the photonic polarization vector $\vec{u}_{i,\vec{q}}(\vec{r})$ is a lattice periodic function in the x - y plane and localized around the slab in the z direction. It can be decomposed into a Fourier series as

$$\vec{u}_{i,\vec{q}}(\vec{r}) = \sum_n \vec{u}_{i,\vec{q},\vec{G}_n}(z) e^{i\vec{G}_n\cdot\vec{\rho}}, \quad (3)$$

where $\vec{G}_n = \frac{2\pi}{a}(n_1, n_2)$ is the 2D reciprocal lattice vector with n_1 and n_2 being integers. The field is normalized such that

$$S^{-1} \int d\vec{\rho} dz \varepsilon(\vec{r}) |\vec{u}_{i,\vec{q}}(\vec{r})|^2 = 1 \quad (4)$$

with $\varepsilon(\vec{r})$ the coordinate-dependent relative dielectric function. Both $\omega_{i,\vec{q}}$ and $\vec{u}_{i,\vec{q}}(\vec{r})$ are calculated via the plane wave expansion method [46].

B. QW excitons

We consider excitons in [001]-grown GaAs/AlAs MQWs. The thickness of the AlAs barrier layers is taken to be large enough to suppress the tunneling between QWs. Typically the width of the GaAs QW is around 5 nm and the thickness of the AlAs barrier is 3 or 4 nm. In this way excitons in each QW can be regarded as independent and then coupled to the 2D photonic bands collectively. For narrow QWs we adopt the approximation to include only the lowest electron and hole subbands since other subbands have much higher energy. The subbands are calculated using the standard method in Ref. [48] with band parameters taken from the semiconductor handbooks [50,51]. We apply the parabolic dispersion approximation for the electron and hole subbands with the higher order in \vec{k} terms neglected (they have been shown to be unimportant in Ref. [53]). The spectra of the conduction band electron and valence band hole are then expressed as $E_{e,\vec{k}} = \frac{\hbar^2 k^2}{2m_e}$ and $E_{h,\vec{k}} = \frac{\hbar^2 k^2}{2m_h}$, respectively. In [001]-grown GaAs QWs the lowest-hole subband is the heavy-hole subband with spin $\pm\frac{3}{2}$ [49]. The valence band mixing in the Luttinger Hamiltonian [54] induces considerable modification of the heavy-hole effective mass in the QW plane m_h [49] which has been taken into account in this work using perturbation theory [49] (Appendix B). The exciton Hamiltonian is constructed by taking into account the electron-hole Coulomb interaction in the subband basis,

$$H_{\text{ex}} = -\frac{\hbar^2 \partial_{\vec{\rho}_e}^2}{2m_e} - \frac{\hbar^2 \partial_{\vec{\rho}_h}^2}{2m_h} + V_{QW}(\vec{\rho}_e - \vec{\rho}_h) + E_g + E_{1e} + E_{1h}, \quad (5)$$

where E_g , E_{1e} , and E_{1h} are the band gap of GaAs, the quantization energy of the first electron subband, and that of the first hole subband, respectively. The effective Coulomb potential is

$$V_{QW}(\vec{\rho}_e - \vec{\rho}_h) = -\int \frac{dz_e dz_h e^2 |\xi_c(z_e)|^2 |\xi_v(z_h)|^2}{4\pi \epsilon_0 \epsilon \sqrt{(\vec{\rho}_e - \vec{\rho}_h)^2 + (z_e - z_h)^2}}, \quad (6)$$

where ξ_c and ξ_v are the wave functions of the electron and hole subbands, respectively. The exciton Hamiltonian can be separated into the center-of-mass and the relative motion parts. The former describes the free motion of the exciton whereas the latter resembles the 2D hydrogen atom system. The exciton energy and wave function are calculated by diagonalizing the above Hamiltonian numerically. The energy of the p th s -orbit exciton state is written as

$$E_{\text{ps}}(\vec{q}) = E_{\text{ps}} + \frac{\hbar^2 q^2}{2m_X}, \quad (7)$$

where E_{ps} is the energy of the excitonic state at $\vec{q} = 0$ and $m_X = m_e + m_h$ is the exciton effective mass. The calculated $1s$ exciton recombination energy, 1.613 eV, for QWs of width 7 nm and barrier width 3 nm, agrees fairly well with the experimental data of 1.6116 eV in Ref. [8].

C. Exciton-photon interactions

Excitons in the MQWs interact with the 2D photonic bands via electric dipole interactions. The Hamiltonian describing such interaction is constructed by exploiting momentum

conservation in the x - y plane. Due to the lattice translation symmetry of the PhC, two wave vectors with a difference of a reciprocal lattice vector \vec{G}_n are equivalent. A model Hamiltonian based on those features was established in Refs. [31,32] for the single-QW case. Here, we extend the theory to the MQW case (Appendix C). The final form of the Hamiltonian is

$$H = H_X + H_P + H_{\text{int}}, \quad (8a)$$

$$H_X = \sum_{l,\alpha,p,n,\vec{q}} E_{\text{ps}}(\vec{q} + \vec{G}_n) \beta_{l,\alpha,p,\vec{q}+\vec{G}_n}^\dagger \beta_{l,\alpha,p,\vec{q}+\vec{G}_n}, \quad (8b)$$

$$H_P = \sum_{i,\vec{q}} \hbar \omega_{i,\vec{q}} a_{i,\vec{q}}^\dagger a_{i,\vec{q}}, \quad (8c)$$

$$H_{\text{int}} = \sum_{l,\alpha,p,n,i,\vec{q}} i \hbar \bar{\Omega}_{l,\alpha,p,n,i,\vec{q}} \beta_{l,\alpha,p,\vec{q}+\vec{G}_n}^\dagger a_{i,\vec{q}} + \text{H.c.} \quad (8d)$$

Here H_X and H_P are the Hamiltonian of the exciton and photon, respectively. $\beta_{l,\alpha,p,\vec{q}+\vec{G}_n}^\dagger$ creates an exciton in the l th QW in the p th s orbit with center-of-mass wave vector $\vec{q} + \vec{G}_n$ of polarization α . $a_{i,\vec{q}}^\dagger$ creates a photon in the i th 2D photonic band with Bloch wave vector \vec{q} . We assume that all the QWs are of the same width and hence the same E_{ps} (we will discuss the fluctuation of E_{ps} later). The index l labels the l th QW. $\alpha = L, T$ stands for the longitudinal or transverse exciton of which the polarization (in the QW plane) is along or perpendicular to its wave vector [55]. The energy difference between the longitudinal and transverse excitons in GaAs QWs is caused by two factors: the short-range interaction due to interband Coulomb interaction and the long-range interaction due to the coupling with photons [56,57]. The latter, which is the central focus of this work, is described by H_{int} , whereas the former is negligible for GaAs QW excitons [56,57]. We thus ignore the dependence of polarization on the exciton energy, as expressed in Eq. (8b). The exciton-photon coupling $\bar{\Omega}_{l,\alpha,p,n,i,\vec{q}}$ is given by (see Appendix C for details)

$$\bar{\Omega}_{l,\alpha,p,n,i,\vec{q}} = \frac{|\phi_p(0)| d \sqrt{\omega_{i,\vec{q}}}}{\sqrt{2\hbar \epsilon_0}} \times \left[S_{\text{uc}}^{-1} \int_{\text{uc}} d\vec{\rho} e^{-i\vec{G}_n \cdot \vec{\rho}} u_{\alpha,i,\vec{q}}(\vec{\rho}, z_l) \right]. \quad (9)$$

$|\phi_p(0)|$ is the amplitude of the p th s -orbital excitonic wave function when the distance between electron and hole is zero. In Appendix F we show that the contribution to the lower polariton branch mainly comes from the $1s$ exciton states, while other s orbits can be ignored. Hereafter we replace the index p with $1s$ (or omit it if possible). d is the interband dipole matrix element in GaAs. z_l is the coordinate of the center of the l th QW in the z direction. $S_{\text{uc}} = a^2$ is the area of the unit cell of the PhC in the x - y plane. $u_{\alpha,i,\vec{q}} = \vec{e}_\alpha \cdot \vec{u}_{i,\vec{q}}$ where $\vec{u}_{i,\vec{q}}$ is the periodic Bloch wave function of the i th photonic band with Bloch wave vector \vec{q} [see Eq. (2)] and \vec{e}_α is the polarization direction of the α exciton. For longitudinal ($\alpha = L$) excitons \vec{e}_α is along \vec{q} , while for the transverse ($\alpha = T$) exciton it is perpendicular to both \vec{q} and the z direction. The integration in Eq. (9) is performed within a unit cell (uc) of the PhC in the x - y plane.

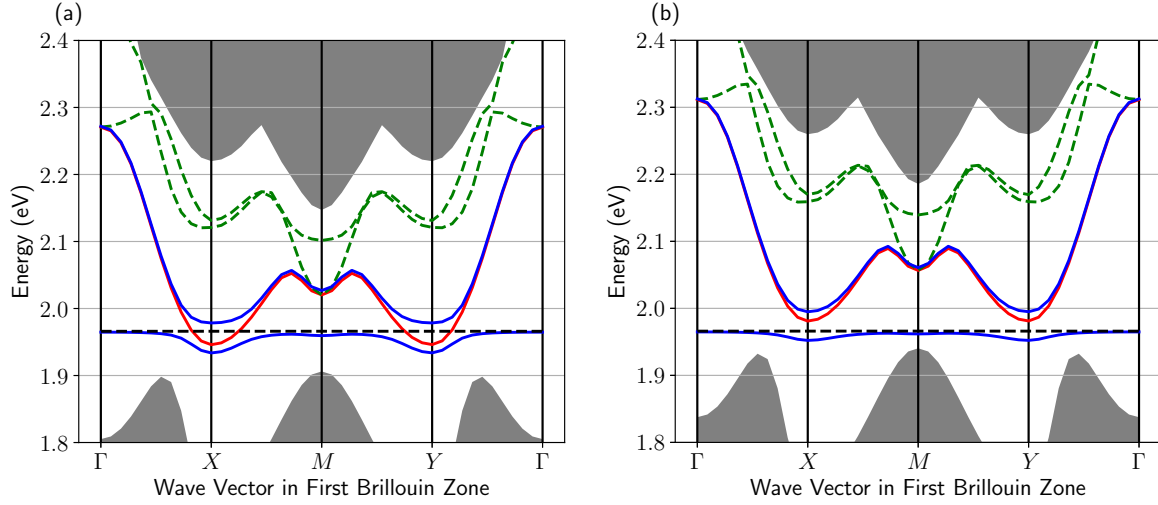


FIG. 2. Dispersion of the confined photonic bands (red [solid] and green [dashed] curves), the exciton (black [dashed] curve), and the lower and upper polariton branches (blue solid curves below the exciton band and above the lowest confined photonic band, respectively). The bulk photonic bands are indicated by the gray (shaded) regions. The detuning between the exciton and the lowest confined photonic band (red solid curve) is (a) $\Delta_{\vec{Q}^{(x)}} = 20$ meV and (b) $\Delta_{\vec{Q}^{(x)}} = -15$ meV. The case (a) of positive detuning is more favorable to high-temperature polariton BEC. The exciton recombination energy is $E_{1s} = 1.966$ eV. The collective exciton-photon coupling is $\hbar\Omega_{\vec{Q}^{(x)}} = 20$ meV. Those two parameters correspond to the situation with QW width 2 nm and barrier layer width 4 nm. The detuning can be achieved by setting the in-plane lattice constant of the PhC as $a = 267$ nm for (a) and $a = 263$ nm for (b). The lower polariton is more photonlike in (a) compared to (b).

D. Polaritons

In the above formulation, \vec{q} is defined in the first Brillouin zone, i.e., $q_x, q_y \in [-\frac{\pi}{a}, \frac{\pi}{a})$. Since the effective mass of the exciton is about four orders of magnitude larger than that of the cavity photon, the excitonic density of states is much larger than the photonic ones. Hence the higher photonic bands are rarely populated (see Appendix F). What is crucial for polariton BEC is the dispersion of the lower polariton branch. For positive detuning, the lower polariton dispersion inherits the photonic dispersion only in the small wave vector range when the photonic energy is lower than the excitonic energy [see Figs. 1(b) and 2]. Beyond that range, the lower polariton branch becomes excitonlike. We focus on small positive detuning $\Delta_{\vec{Q}^{(x)}} \equiv E_{1s} - \hbar\omega_0^{(x)}$ where only the dispersion close to the energy minima of the lowest 2D photonic band is relevant (see Fig. 2). Here, we have employed the sign convention for the exciton-photon detuning which is opposite of that traditionally found in the literature. In this situation, we approximate the dispersion of the photonic band entirely by Eq. (1) and omit the index i . The lower polariton branch dispersion E_{LP} is obtained by diagonalizing the Hamiltonian Eq. (8a) under these approximations. Direct calculation yields (see Appendix C)

$$\sum_{l,\alpha,n} \frac{\hbar^2 |\bar{\Omega}_{l,\alpha,n,\vec{q}}|^2}{(E_{LP} - \hbar\omega_{\vec{q}})[E_{LP} - E_{1s}(\vec{q} + \vec{G}_n)]} = 1. \quad (10)$$

Since the magnitudes of the relevant \vec{G}_n are too small to induce a considerable difference in exciton energy one can use the approximation $E_{1s}(\vec{q} + \vec{G}_n) \simeq E_{1s}(\vec{q})$ (i.e., the photonic wavelength is much larger than the thermal de Broglie wavelength of exciton). The solution to Eq. (10) then gives the

simple form of

$$E_{LP}(\vec{q}) = \frac{E_{1s}(\vec{q}) + \hbar\omega_{\vec{q}}}{2} - \left[\left(\frac{E_{1s}(\vec{q}) - \hbar\omega_{\vec{q}}}{2} \right)^2 + \hbar^2 \Omega_{\vec{q}}^2 \right]^{\frac{1}{2}}, \quad (11)$$

where $\hbar\Omega_{\vec{q}} = \hbar\sqrt{\sum_{l,\alpha,n} |\bar{\Omega}_{l,\alpha,n,\vec{q}}|^2}$ is referred to as the collective exciton-photon coupling. We further approximate $\Omega_{\vec{q}}$ as its value at $\vec{Q}^{(x)}$ or $\vec{Q}^{(y)}$ since only the coupling around those photonic energy minima is relevant. According to the D_{2d} symmetry of the symmetric-woodpile structure, $\Omega_{\vec{Q}^{(x)}} = \Omega_{\vec{Q}^{(y)}} \equiv \Omega$. The effective Hamiltonian for polaritons can then be simplified to [31,32]

$$H = H_0 + H_I, \quad (12a)$$

$$H_0 = \sum_{\vec{q}} [E_{1s}(\vec{q}) b_{\vec{q}}^\dagger b_{\vec{q}} + \hbar\omega_{\vec{q}} a_{\vec{q}}^\dagger a_{\vec{q}}], \quad (12b)$$

$$H_I = \sum_{\vec{q}} i\hbar\Omega (b_{\vec{q}}^\dagger a_{\vec{q}} - a_{\vec{q}}^\dagger b_{\vec{q}}), \quad (12c)$$

with the help of the collective excitonic operator [28]

$$b_{\vec{q}} \equiv \sum_{l,\alpha,n} \frac{\Omega_{l,\alpha,n,\vec{q}}}{\Omega_{\vec{q}}} \beta_{l,\alpha,n,\vec{q}}. \quad (13)$$

The above operator is a linear combination of exciton operators with largest coupling to the photon. Other orthogonal combinations interact only weakly with the lowest 2D photonic band.

The spectra of the confined 2D photonic bands and the polaritons are illustrated in Fig. 2. Specifically we plot for both positive [Fig. 2(a)] and negative [Fig. 2(b)] detuning $\Delta_{\vec{Q}^{(x)}}$ cases. It is seen that away from the X point [i.e., $\vec{Q}^{(x)} = (\frac{\pi}{a}, 0)$, one of the energy minima] the lower polariton dispersion is almost flat because the excitonic effective mass is much

larger than the photonic one. The lower polariton branch at positive detuning has a deeper dispersion and smaller effective mass which leads to higher temperature polariton BEC compared with the negative detuning case [13,28]. Accordingly, we focus on positive detuning in the following discussions. To ensure the approximation on the photonic dispersion, Eq. (1), the exciton recombination energy must be close to the photonic band edge. In this system it requires $\Delta_{\vec{Q}^{(x)}} \leq 40$ meV to avoid nonparabolic photonic dispersion (see Appendix F for details). In addition, there are physical trade-offs for choosing $\Delta_{\vec{Q}^{(x)}}$: For large positive detuning, the lower polariton dispersion depth becomes very large and the effective mass of the lower polariton becomes very small, but the lower polariton becomes more photonlike. This implies that the phonon-polariton and polariton-polariton interactions become much weaker. This implies a much longer time for polaritons to relax down to the ground states, to thermalize, and to reach equilibrium polariton BEC.

III. POLARITON BEC TOY MODEL FOR TWO DISPERSION MINIMA

As depicted in Fig. 1, in the symmetric-woodpile system, there are two degenerate lower polariton ground states. In other asymmetric architectures, such as the slanted-pore system (see Sec. VB), this degeneracy is lifted due to symmetry breaking. In the previous subsection, we derived the polariton dispersion and an effective Hamiltonian for an exciton coupled to the guided photonic band. In the photonic dispersion of the guided band there are two local minima, one at $\vec{Q}^{(x)}$ and another at $\vec{Q}^{(y)}$. In the symmetric-woodpile structure, these two minima are degenerate in energy while in the slanted-pore system, or an asymmetric-woodpile system (i.e., one where $w_x \neq w_y$ and $h_x \neq h_y$) (see Sec. VB), the two minima may be nondegenerate. In this section, we construct a toy model for a polariton with two nondegenerate minima. In a real system, exciton-exciton interactions would provide coupling between the two minima and break the ground-state degeneracy. In our noninteracting toy model, polaritons may distribute themselves between the two degenerate (single-particle) minima, halving the density relevant to BEC and substantially decreasing the critical temperature. We find, instead, that due to the very large and proximal excitonic density of states, the double minimum causes only a small reduction in the critical temperature for realistic parameters. Our toy model reveals that a substantial difference in BEC onset temperature would occur only for unphysical parameter values in our system. On the other hand, the occupation of excitonlike states decreases exponentially as the temperature is lowered below the onset of BEC. As a result, a high condensate fraction ($\sim 50\%$) is more readily achieved with a small amount of symmetry breaking.

A. Toy model

To construct a polariton dispersion with two minima, we begin by treating the photonic dispersion around each minima at $\vec{Q}^{(x)}$ or $\vec{Q}^{(y)}$ as separate bands with a dispersion similar to Eq. (1). This approximation is justified because for regions of q space where the photonic energy exceeds the excitonic energy, the polariton dispersion is very excitonlike. Therefore,

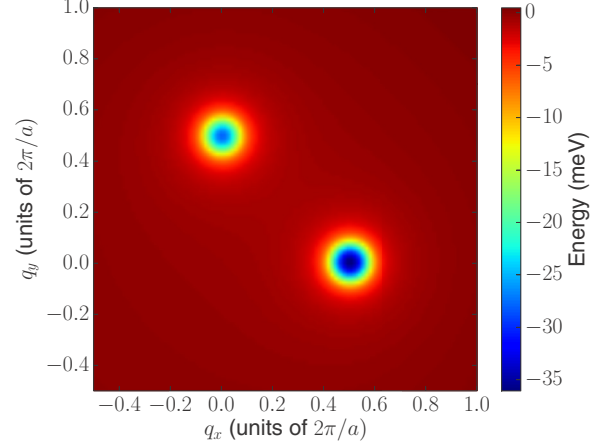


FIG. 3. The polariton dispersion with two minima given by the toy model in Eq. (15). We take $a = 250$ nm as the in-plane lattice constant. The (density of states) photonic effective mass at $\vec{Q}^{(x)} = (0.5, 0)\frac{2\pi}{a}$ and $\vec{Q}^{(y)} = (0, 0.5)\frac{2\pi}{a}$ are $m_{\text{ph}}^{(x)} = m_{\text{ph}}^{(y)} = 5 \times 10^{-6}m_0$ and $m_{\text{exc}} = 0.176m_0$. The exciton-photon coupling strengths are $\hbar\Omega_{\vec{Q}^{(x)}} = \hbar\Omega_{\vec{Q}^{(y)}} = 15$ meV. The detunings are $\Delta_{\vec{Q}^{(x)}} = 30$ meV and $\Delta_{\vec{Q}^{(y)}} = 20$ meV.

it is only the regions of q space where the photonic dispersion is below that of the exciton that are of importance for polariton dynamics. We then consider each band to be coupled to the exciton, yielding each a polariton band centered around either $\vec{Q}^{(x)}$ or $\vec{Q}^{(y)}$. The polariton band centered around \vec{Q} (dropping the ν superscript) can be written as

$$L_{\vec{Q}}(\vec{q}; \Delta_{\vec{Q}}, \Omega_{\vec{Q}}) = \frac{1}{2} \left\{ P(\vec{q} - \vec{Q}; \Delta_{\vec{Q}}) + X(\vec{q}) - \sqrt{[X(\vec{q}) - P(\vec{q} - \vec{Q}; \Delta_{\vec{Q}})]^2 + 4\hbar^2\Omega_{\vec{Q}}^2} \right\}, \quad (14a)$$

$$P(\vec{q}; \Delta) = \frac{\hbar^2}{2m_{\text{ph}}} q^2 - \Delta, \quad (14b)$$

$$X(\vec{q}) = \frac{\hbar^2}{2m_{\text{exc}}} q^2, \quad (14c)$$

where $\Delta_{\vec{Q}} \equiv [X(\vec{q}) - P(\vec{q} - \vec{Q})]_{\vec{q}=\vec{Q}}$ is the exciton-photon detuning for the photonic band centered at \vec{Q} and $\Omega_{\vec{Q}}$ is the light-matter coupling strength evaluated at \vec{Q} . The toy polariton dispersion with two minima is

$$L(\vec{q}) = L_{\vec{Q}^{(x)}}(\vec{q}; \Delta_{\vec{Q}^{(x)}}, \Omega_{\vec{Q}^{(x)}}) + L_{\vec{Q}^{(y)}}(\vec{q}; \Delta_{\vec{Q}^{(y)}}, \Omega_{\vec{Q}^{(y)}}). \quad (15)$$

Through the parameters $\Delta_{\vec{Q}^{(i)}}$, we can adjust the splitting between the two photonic minima and model the polaritonic minima that occur both in the slanted-pore and woodpile systems. We depict a typical polariton dispersion with two minima in Fig. 3.

To compute the critical temperature with this toy dispersion, we consider the polaritons to be trapped in a 2D box of side length D . This trapping induces a discretization of the polariton spectrum in increments of π/D in both the q_x and q_y directions. The wave function for polaritons

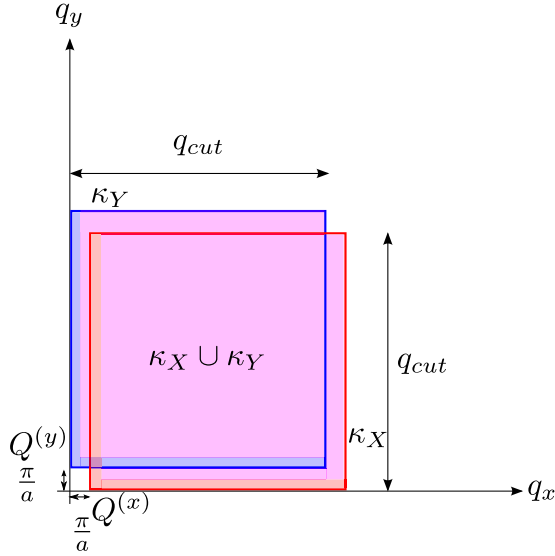


FIG. 4. A schematic diagram showing the regions of \vec{q} space considered in the computation of the critical temperature in Eq. (16). The regions extending from the minima at $\vec{Q}^{(x)} = (\pi/a, 0)$ and $\vec{Q}^{(y)} = (0, \pi/a)$ are labeled κ_X and κ_Y , respectively. The shaded union set $\kappa_X \cup \kappa_Y$ represents the range of momenta allowed by the two-dimensional box trap.

trapped near the dispersion minimum at $\vec{Q}^{(v)}$ is $\psi_{\vec{Q}^{(v)}} \sim e^{iQ_x^{(v)}x} e^{iQ_y^{(v)}y} \sin(q_{n_1}x) \sin(q_{n_2}y)$ where $q_{n_1} = \frac{n_1\pi}{D}$, $q_{n_2} = \frac{n_2\pi}{D}$ for positive integers n_1 and n_2 . Taking the total polariton density to be ρ_{pol} , the number of polaritons in the system is $N = \rho_{\text{pol}}D^2$. We estimate the “transition” (crossover) temperature by the condition that there are fN particles in the ground state (or in each of the ground states, in the case of a degeneracy) with $0 \leq f \leq 1$. There are several criteria to specify the crossover temperature, such as that by Ketterle and van Druten [58] ($f = 0$) or that by Penrose and Onsager [3] ($f = 0.1$). In this work, we focus on the Penrose-Onsager criterion. To compute the critical temperature T_c , we use the following equation:

$$N = N_0^{(x)} + N_0^{(y)} + \sum_{\vec{q} \in \kappa_X \cup \kappa_Y} \left[\exp\left(\frac{L(\vec{q}) - \mu}{k_B T_c}\right) - 1 \right]^{-1}, \quad (16)$$

where

$$N_0^{(v)} = \left[\exp\left(\frac{L(\vec{Q}^{(v)} + \vec{q}_0) - \mu}{k_B T_c}\right) - 1 \right]^{-1}.$$

In Eq. (16), $\vec{q}_0 = (\pi/D, \pi/D)$ and $\kappa_v = \{\vec{q} = \vec{Q}^{(v)} + (n_x, n_y)\frac{\pi}{D} : 1 < n_x, n_y \leq M\}$ represents the discrete regions of \vec{q} space that are permitted by the box trap around each minimum, depicted in Fig. 4. M is the integer such that $M\frac{\pi}{D} = q_{\text{cut}}$ corresponding to the high-momentum cutoff, arising from the finite size of both the box trap and the exciton. Momenta greater than q_{cut} probe the internal structure of the exciton and are not physically relevant (see Appendix E). $N_0^{(v)}$ represents the number of particles in the lowest allowed energy state in each polariton valley. The sum within the intersection set $\kappa_X \cap \kappa_Y$ is performed to ensure that polariton states are not double counted.

B. Two degenerate polariton minima

We first investigate how the critical temperature $T_c^{(2)}$ for a polariton with two dispersion minima differs from the critical temperature $T_c^{(1)}$ with only a single dispersion minimum. We choose realistic parameters (exciton mass, photonic mass, exciton-photon coupling, etc.). For a polariton with a single dispersion minimum, the critical temperature is computed using Eq. (16), setting $N_0^{(y)}$ to zero, and replacing the sum over $\kappa_X \cup \kappa_Y$ with a simple sum over κ_X . We depict our results in Fig. 5. These results indicate that for either the Ketterle–van Druten or Penrose–Onsager criterion, the reduction in critical temperature, $T_c^{(1)} - T_c^{(2)}$, due to the second minimum is on the order of 5 K. The difference in critical temperature increases for larger condensate fractions f . The surprisingly small reduction in T_c for small f is due to the large excitonic density of states above the polariton dispersion minimum. For room-temperature onset of BEC, there is non-negligible occupation of the excitonic states. This occupation limits the influence of a secondary polariton dispersion minimum on the BEC critical temperature. At lower temperatures, the excitonic occupation drops and the presence of a nearly degenerate minimum strongly influences the occupation of the ground state.

To elucidate this effect, we consider (artificially) reducing the excitonic mass which, in turn, reduces the excitonic density of states. By reducing the excitonic mass such that $m_{\text{exc}} \rightarrow m_{\text{ph}}$, the polariton bands approach perfect parabolas, for which

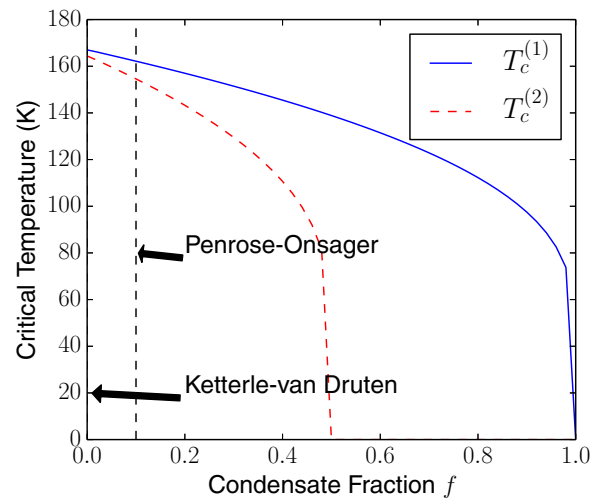


FIG. 5. Critical temperatures $T_c^{(1)}$ and $T_c^{(2)}$ for polariton dispersions with a single minimum (blue [solid] curve) and two degenerate minima (red [dashed] curve), respectively, as a function of condensate fraction f . The box trap side length is $D = 10 \mu\text{m}$; the total polariton density is $\rho_{\text{pol}} = (5a_B)^{-2} = 494 \mu\text{m}^{-2}$ with an exciton Bohr radius of $a_B = 9 \text{ nm}$. The detuning is $\Delta_{\vec{Q}^{(x)}} = \Delta_{\vec{Q}^{(y)}} = 30 \text{ meV}$, the exciton-photon coupling is $\hbar\Omega_{\vec{Q}^{(x)}} = \hbar\Omega_{\vec{Q}^{(y)}} = 15 \text{ meV}$, the (density of states) photonic effective mass is $m_{\text{ph}}^{(x)} = m_{\text{ph}}^{(y)} = 5 \times 10^{-6} m_0$, and the exciton mass is $m_{\text{exc}} = 0.176 m_0$. The in-plane photonic-crystal lattice constant is assumed as $a = 250 \text{ nm}$, and the high-momentum cutoff is $q_{\text{cut}} = 2\pi/a_B$. The vertical (dashed) lines at $f = 0$ and $f = 0.1$ represent the condensate fractions of the Ketterle–van Druten and Penrose–Onsager criteria. At $f = 0.5$, $T_c^{(2)} \rightarrow 0$ since all noninteracting polaritons have condensed equally into the two degenerate ground states.

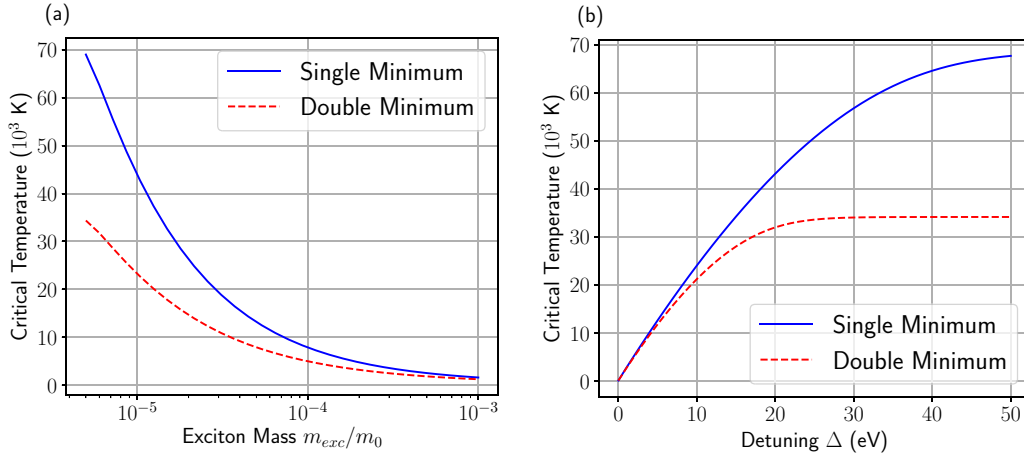


FIG. 6. (a) Critical temperature for a polariton dispersion with a single dispersion minimum (blue [solid] curve) and two dispersion minima (red [dashed] curve) as a function of exciton mass m_{exc} , in units of the bare electron mass in vacuum m_0 . All other parameters are the same as in Fig. 5. (b) Critical temperature for a polariton dispersion with a single dispersion minimum (blue [solid] curve) and two dispersion minima (red [dashed] curve) as a function of exciton-photon detuning $\Delta \equiv \Delta_{\vec{Q}^{(x)}} = \Delta_{\vec{Q}^{(y)}}$. All other parameters are the same as those in Fig. 5.

we expect that $T_c^{(2)} \rightarrow \frac{1}{2}T_c^{(1)}$. This behavior is confirmed in Fig. 6(a). Another way to artificially displace the large exciton density of states is to increase the exciton-photon detuning so much that the polariton over the entire q range (up to the q cut-off) is very photonlike. Here, we likewise expect $T_c^{(2)} \rightarrow \frac{1}{2}T_c^{(1)}$, since both the polariton bands are almost completely parabolic. Figure 6(b) shows that this occurs only for extremely large and unphysical detunings of about 5×10^4 meV. For realistic physical values of the exciton mass, exciton-photon detuning, and coupling strengths, the critical temperature for $f = 0.1$ is modified only by about 5 K, due to the large and proximal density of excitonlike states. For larger choices of the condensate fraction, f , the temperature must be lowered and the occupation of the excitonlike states is less prominent. In this case, the difference between $T_c^{(2)}$ and $T_c^{(1)}$ is more pronounced.

In our toy model, we consider only noninteracting excitons. In reality, exciton-exciton interactions lead to scattering of polaritons between the two dispersion minima at $\vec{Q}^{(x)}$ and $\vec{Q}^{(y)}$ and a lifting of the degeneracy of the polariton ground state. For example, the true (nondegenerate) ground state may consist of a coherent many-body state composed of a linear combination of the $\vec{Q}^{(x)}$ and $\vec{Q}^{(y)}$ single-polariton states. More exotic (fragmented) quantum many-body states may also occur depending on the detailed nature of the exciton-exciton interactions [59].

C. Symmetry breaking of the photonic-crystal cavity modes

We now investigate the efficacy of symmetry breaking to lift the polariton dispersion degeneracy and improve $T_c^{(2)}$. To gain physical understanding, we start with a limiting case of unphysical large detunings of $\Delta = \Delta_{\vec{Q}^{(x)}} = \Delta_{\vec{Q}^{(y)}} = 5 \times 10^4$ meV. This creates essentially parabolic polariton dispersions for all relevant wave vectors and at $f = 0.1$, $T_c^{(2)} = \frac{1}{2}T_c^{(1)}$. It is instructive to consider how $T_c^{(2)}$ changes with asymmetry $S \equiv \Delta_{\vec{Q}^{(x)}} - \Delta_{\vec{Q}^{(y)}}$ for $\Delta_{\vec{Q}^{(x)}}$ fixed at 50 eV. In this unphysical scenario, $k_B T_c^{(1)} \approx 7 \times 10^3$ meV. A simple calculation confirms that for an asymmetry of $S = \Delta_{\vec{Q}^{(x)}} - \Delta_{\vec{Q}^{(y)}} \approx 7$ eV, $T_c^{(2)} \rightarrow$

$T_c^{(1)}$. As expected, in the absence of excitonlike states, the degeneracy of the two minima must be lifted by about $k_B T_c^{(1)}$ before the second shallower minimum no longer influences $T_c^{(2)}$.

The situation is quite different for realistic, physical parameters with a large, proximal, excitonic density of states. We plot the critical temperature for a polariton dispersion with two minima, with $\Delta_{\vec{Q}^{(x)}} = 30$ meV and $0 \leq S \leq 1$ meV, as a function of photonic asymmetry S . Figure 7 reveals an initial rapid increase of $T_c^{(2)}$ with asymmetry that saturates to about 5 K at an asymmetry of $S \sim 0.3$ meV. The large proximal excitonic density of states limits any further influence of asymmetry on $T_c^{(2)}$ for a condensate fraction of $f = 0.1$.

We now consider the case of larger condensate fractions f . This involves lower temperatures where the excitonlike states in the polariton dispersion are much less populated. This regime is important for the exploration of novel quantum many-body states that may arise when exciton-exciton interactions are considered. We define $\Delta T_c = T_c(S = S_{\text{sat}}) - T_c(S = 0)$ where S_{sat} is the photonic asymmetry at which T_c no longer increases significantly. Figure 8 reveals that asymmetry is most influential at large condensate fractions f . The largest ΔT_c occurs for $f = 0.5$, where all (noninteracting) polaritons are assumed to have condensed in the doubly degenerate case. This is similar to the behavior of $T_c^{(1)} - T_c^{(2)}$ seen in Fig. 5. In Fig. 8(b), we note an initial rapid increase in S_{sat} with condensate fraction. This is because for small condensate fractions, a small amount of asymmetry will not dramatically alter the occupation of the ground and first few excited states, since there are so few particles in these states to begin with. S_{sat} increases rapidly again as the condensate fraction approaches unity. In this case, the critical temperature approaches zero.

IV. STRONG-COUPLING AND HIGH-TEMPERATURE POLARITON BEC

A. Strong exciton-photon coupling

The exciton-photon coupling can be controlled by the width of the QW. In Fig. 9(a) we plot such dependence (for details of the calculation see Appendices B and C). It is seen that

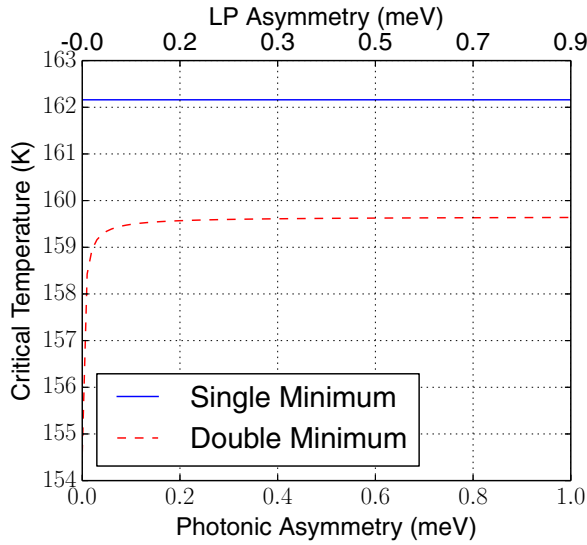


FIG. 7. Critical temperature for a polariton dispersion with two minima (red [dashed] curve) as a function of the splitting $S \equiv \Delta_{\vec{Q}^{(x)}} - \Delta_{\vec{Q}^{(y)}}$ between the two photonic minima. The upper x axis indicates the splitting between the two polariton minima, i.e., $L(\vec{Q}^{(y)}) - L(\vec{Q}^{(x)})$. The detuning $\Delta_{\vec{Q}^{(x)}} = 30$ meV, and $\Delta_{\vec{Q}^{(y)}} = \Delta_{\vec{Q}^{(x)}} - S$. All other parameters are the same as in Fig. 5. The condensate fraction is taken as $f = 0.1$. The critical temperature for a polariton with a single dispersion minimum at $\vec{Q}^{(x)}$ is shown for comparison (in [solid] blue).

the exciton-photon coupling is enhanced by reducing the QW width. This is mainly for the following reasons. First, for smaller QW widths, more QWs can be placed in the central slab to enhance exciton-photon coupling. Second as the exciton recombination energy E_{1s} is larger for small QW width, the photon energy $\hbar\omega_{\vec{q}}$ is also larger if the detuning is fixed. According to Eq. (9) the coupling is stronger when $\hbar\omega_{\vec{q}}$ is larger. The calculated exciton-photon coupling increases from 12 meV to 20 meV when the QW width reduces from 8 nm to 2 nm. Most of the material parameters used in the calculation are given in the caption of Fig. 9. The effective mass of the electron is $m_e = 0.065m_0$. The hole effective mass is calculated from the Luttinger Hamiltonian [54] numerically

for different QW widths (see Appendix B). The amplitude of the exciton wave function $|\phi_1(0)|$ and the exciton Bohr radius a_B are also calculated for different QW widths. From our calculation, a_B is found to be $\simeq 9$ nm, and $|\phi_1(0)| \simeq a_B^{-1} \sqrt{2/\pi}$ is about $0.9 \times 10^8 \text{ m}^{-1}$ (see Fig. 16 in Appendix B).

In Table I we summarize the main properties of the PhC microcavity in comparison with the FP microcavity. To compare with the experimental results in Ref. [8] which are obtained at low temperature (4 K), the material parameters (such as GaAs and AlAs band gaps) here are taken as for $T = 4$ K. For the same reason the QW width is taken as 7 nm and the barrier layer width is 3 nm. The lowest 2D photonic band edge is set to be in resonance with the exciton recombination energy which is 1.61 eV. In contrast, for all the other calculations in this work, we use the room-temperature material parameters. The material parameters for both 4 K and room temperature are listed in Appendix B. We calculate the photonic field distribution in the FP cavity using the finite difference time domain method [60] from which the exciton-photon coupling is obtained.

Table I shows that the exciton-photon coupling in the PhC cavity is *much stronger* than that in the FP cavity, with an added advantage that fewer QWs are required to obtain strong coupling. To understand this we plot the photonic field intensity distribution along the growth direction in Fig. 9(c). Specifically, the field intensities are for the photon with $\vec{q} = 0$ in the FP cavity or for the photon with $\vec{q} = \vec{Q}^{(x)}$ in the woodpile PhC cavity. The field intensity distribution is asymmetric for the PhC cavity as it does not have the mirror symmetry with respect to the slab. Remarkably, in the central slab region, the average photonic field intensity in the PhC cavity is about 8 times as large as that in the FP cavity. The nonuniformity of PhC microcavity in the x - y plane promotes a nonuniform electric field, with a peak field intensity up to 20 times as large as that in the FP cavity as revealed in Ref. [28]. This significant enhancement is because the PhC cavity focuses the photonic field much more strongly than the FP cavity due to the PBG and the larger dielectric contrast in the PhC microcavity. The collective exciton-photon coupling can be further enhanced by using a slanted-pore crystal with a larger PBG [61] (to be discussed in Sec. V).

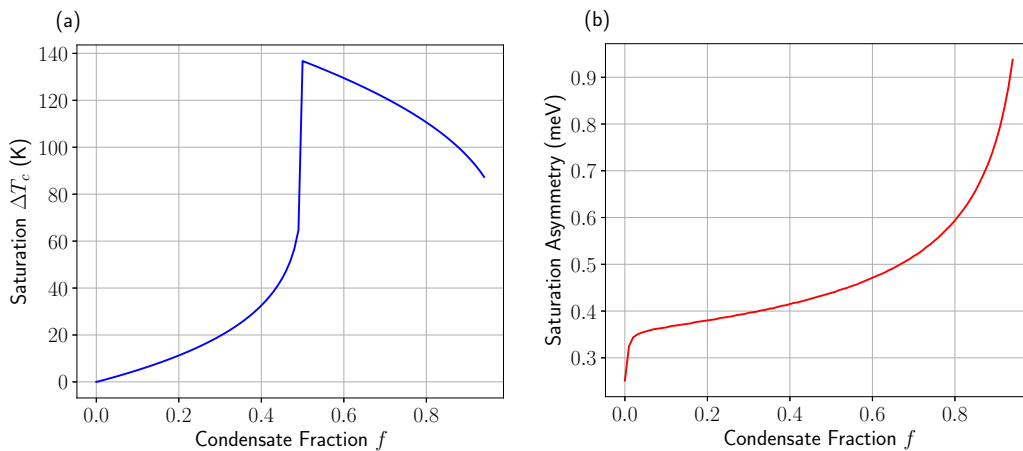


FIG. 8. (a) Saturation change in critical temperature ΔT_c and (b) saturation asymmetry S_{sat} as a function of condensate fraction f . In (a) $\Delta T_c = T_c(S = S_{\text{sat}}) - T_c(S = 0)$ where S_{sat} is depicted in (b). All other parameters are the same as in Fig. 5.

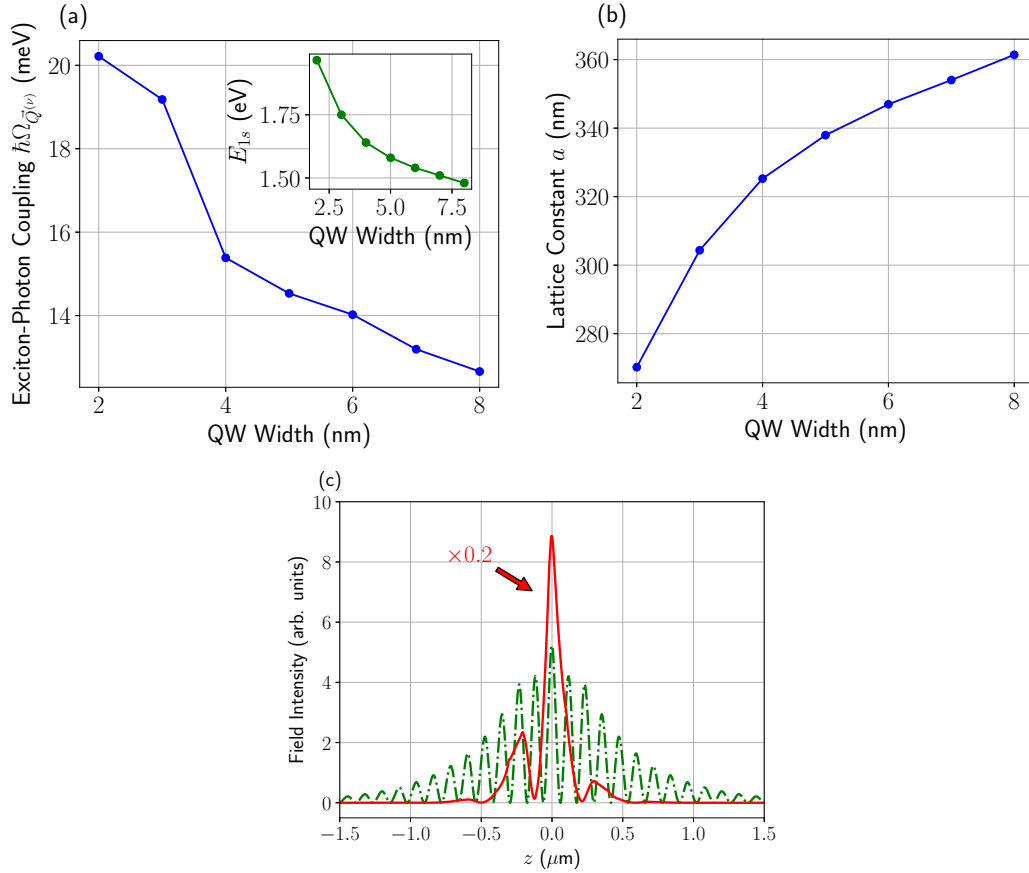


FIG. 9. (a) Collective exciton-photon coupling $\hbar\Omega_{\vec{Q}^{(x)}}$ as a function of the QW width for AlGaAs symmetric-woodpile system. The coupling is evaluated at $\vec{Q}^{(x)}$. The width of the AIAs barrier layers here is fixed at 4 nm. The interband dipole matrix element is $d = 1.1 \times 10^{-28}$ C m. The inset indicates how E_{1s} evolves with the QW width. (b) The in-plane PhC lattice constant a as a function of QW width. The lattice constant varies so as to maintain a fixed detuning of $\Delta_{\vec{Q}^{(x)}} = 40$ meV. (c) Photonic field intensity along the growth direction (in arbitrary units) of the confined photonic band $S^{-1} \int d\vec{\rho} |\vec{\mathcal{E}}(\vec{\rho}, z)|^2$ in the PhC (red [solid]) and FP (green [dash-dotted]) cavities. The values are taken for band-edge photons. Specifically for the FP cavity, $\vec{q} = 0$, and for the woodpile PhC cavity, $\vec{q} = \vec{Q}^{(x)}$. The photonic band edge energy is 1.61 eV for both types of cavity. The in-plane lattice constant for the PhC is $a = 321$ nm. Note that the photon field intensity for the PhC cavity has been multiplied by a factor of 0.2 to plot on the same graph.

B. High-temperature polariton BEC

The BEC transition temperature depends strongly on the polariton density (which is determined by the excitation intensity). We consider the situation where excitons are excited at higher energy states in the beginning and then allowed to relax to the polaritonic ground state. The excitonic fraction, P_l , of the lower polariton in the l th QW is proportional to the coupling between the photon and the exciton in the l th QW

(see Appendix C 2):

$$P_l = \frac{\hbar^2 \Omega_l^2}{(E_{LP} - E_{1s})^2} \left[1 + \sum_l \frac{\hbar^2 \Omega_l^2}{(E_{LP} - E_{1s})^2} \right]^{-1} \quad (17)$$

with $\Omega_l \equiv \sqrt{\sum_{\alpha,n} |\bar{\Omega}_{l,\alpha,n,\vec{Q}^{(x)}}|^2}$. For polariton areal density n , the exciton density in the l th QW is nP_l . nP_l must be smaller

TABLE I. Comparing the properties of the FP and the PhC microcavities when the lowest confined photonic bands in the two cavities are in resonance with the GaAs QW exciton (i.e., $\Delta = 0$) at $T = 4$ K. The QW width is 7 nm, while the barrier layer width is 3 nm. The exciton energy is 1.61 eV, according to Ref. [8]. N is the number of QWs.

	Collective coupling $\hbar\Omega$	Coupling per QW $\frac{\hbar\Omega}{\sqrt{N}}$	Photon lifetime
FP cavity:	7.45 meV (12 QWs) [8]	2.15 meV	~ 10 ps
Woodpile PhC cavity:	13.3 meV (2 QWs)	9.4 meV	$\gtrsim 1$ ns [37,42]

than the exciton saturation density to avoid unbinding of excitons due to many-body (screening and phase-space filling) effects [62]. For a single GaAs QW the exciton saturation density is $(5a_B)^{-2}$ where a_B is the Bohr radius. In MQWs, an areal polariton density $n \leq n_m \equiv (5a_B)^{-2}/\max(P_l)$ is required, where $\max(P_l)$ is the maximal value of P_l among all QWs. If the QW width is 2 nm, the collective coupling strength (for three QWs in the central slab) is $\hbar\Omega_{\tilde{Q}^{(s)}} = 20.2$ meV for a woodpile system with a $0.07a$ central slab, assuming a detuning $\Delta_{\tilde{Q}^{(s)}} = 40$ meV (with an in-plane lattice constant of $a = 270$ nm). This yields $n_m = 1.0 \times 10^4 \mu\text{m}^{-2}$ in both the woodpile and slanted-pore architectures. In our calculation we take polariton densities less than $n_m/4 = (10a_B)^{-2}/\max(P_l)$.

Following Ref. [28] we define the dispersion depth of the lower polariton branch as the energy difference between the polariton dispersion minima and the exciton band edge. With detuning $\Delta_{\tilde{Q}^{(v)}}$, the polariton dispersion depth is given by

$$V_{\tilde{Q}^{(v)}} \equiv E_{1s} - E_{LP}(\tilde{Q}^{(v)}) = \frac{\Delta_{\tilde{Q}^{(v)}}}{2} + \sqrt{\left(\frac{\Delta_{\tilde{Q}^{(v)}}}{2}\right)^2 + \hbar^2\Omega_{\tilde{Q}^{(v)}}^2}, \quad (18a)$$

$$V = \max\{V_{\tilde{Q}^{(s)}}, V_{\tilde{Q}^{(v)}}\}. \quad (18b)$$

Physically, V characterizes the energy range of the polariton dispersion with small effective mass. It has been shown in Ref. [28] that the BEC transition temperature T_c is limited by V because for temperatures above V/k_B quasiparticles are mainly populated on excitonlike states. BEC, in this situation, requires a density much higher than n_m . Positive detuning $\Delta_{\tilde{Q}^{(s)}} > 0$ enables larger dispersion depths and higher T_c . However, for large detuning, low-energy polaritons are more photonlike. The resulting weak polariton-phonon and polariton-polariton interaction strengths lead to small scattering rates and the polariton gas requires a longer time to achieve thermodynamic equilibrium. Since we consider only small positive detunings less than 40 meV in this work, the maximum excitonic fraction in any single QW of the polariton, $\max P_l$, is considerable (ranging from 4% to 17%), thanks to the strong exciton-photon coupling in the PhC microcavity.

We calculate the transition temperature T_c for two polariton densities with various QW width and a fixed detuning $\Delta_{\tilde{Q}^{(s)}} = 40$ meV in Fig. 10. T_c is decreased with increasing QW width because the collective exciton-photon coupling $\hbar\Omega_{\tilde{Q}^{(s)}}$ is reduced [see Fig. 9(a)]. The increase in T_c at a quantum well width of 3 nm can be explained as follows. For both well widths of 2 nm and 3 nm, there are three quantum wells in the central slab. The coupling strength is slightly smaller for the 3 nm case, due to the decreased exciton recombination energy. This results in more photonlike polaritons and allows for a larger polariton density which causes higher critical temperatures. However, for a well width of 4 nm, the system can accommodate only two quantum wells, which causes a decrease in light-matter coupling strength. Moreover, since the excitonic component is distributed over fewer quantum wells, the polaritons are more excitonlike, which results in lower critical temperatures. The results plotted in Fig. 10 demonstrate the possibility of high-temperature ($T_c \gtrsim 300$ K) polariton BEC well below the exciton saturation density.

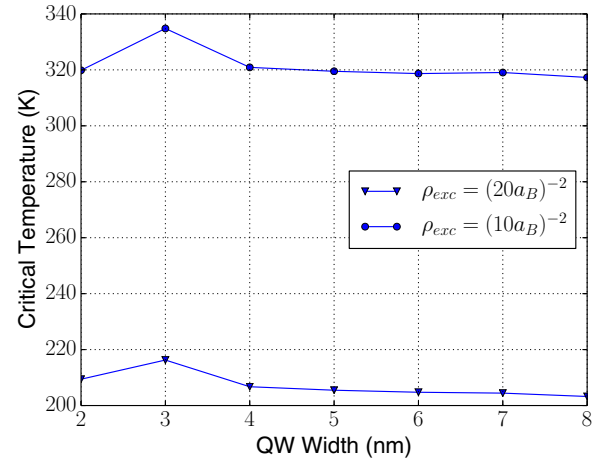


FIG. 10. QW width dependence of the polariton BEC transition temperature T_c for polariton densities $(10a_B)^{-2}/\max(P_l)$ [the curve with circles, corresponding to polariton density of $n = (2.2a_B)^{-2} = 2.6 \times 10^3 \mu\text{m}^{-2}$ for 2 nm MQWs] and $(20a_B)^{-2}/\max(P_l)$ [the curve with triangles, corresponding to $n = (4.3a_B)^{-2} = 0.64 \times 10^3 \mu\text{m}^{-2}$ for 2 nm MQWs] in the symmetric woodpile system. The cavity is taken to be a square quantum box of length $D = 10 \mu\text{m}$. The detuning is $\Delta_{\tilde{Q}^{(s)}} = 40$ meV for all QW widths. The exciton-photon coupling strength and exciton recombination energies are given in Fig. 9(a), while the PhC lattice constant is given in Fig. 9(b). In this figure, $\rho_{exc} \equiv n \max(P_l)$, representing the maximal exciton density in a single QW.

V. ROAD MAP TO ROOM-TEMPERATURE POLARITON BEC

A. Trapping size, detuning, and density dependencies

We now study how the transition temperature T_c varies with box trap side length D , exciton-photon detuning $\Delta_{\tilde{Q}^{(s)}}$, exciton-photon coupling, and the polariton density in the symmetric-woodpile structure. We begin our analysis with the polariton density $(10a_B)^{-2}/\max(P_l)$. From Fig. 11(a), the dependence of T_c on D is qualitatively different from that of atomic (or excitonic) BEC [58]. First, the transition temperature depends weakly on the trapping size (almost logarithmically). For large D , T_c remains almost unchanged up to a macroscopic scale $D = 1$ cm. Second, the dependence on trapping size is nonmonotonic: at $D \simeq 3 \mu\text{m}$ the transition temperature reaches its maximum. For smaller D , when the quantization energy of the polariton due to the trap (i.e., the energy difference between the first excited state and the ground state) is comparable with or larger than the polariton dispersion depth V , the BEC crosses over from polaritonlike to excitonlike and the BEC transition temperature is thus reduced.

From Fig. 11(a) T_c is enhanced by positive detuning. Figure 11(b) shows that T_c increases with both the detuning $\Delta_{\tilde{Q}^{(s)}}$ and the exciton-photon coupling $\hbar\Omega_{\tilde{Q}^{(s)}}$, which is consistent with the enhanced dispersion depth, V , of the lower polariton. Clearly, high temperature polariton BEC is accessible over a range of realistic parameters. The highest transition temperature reported in this work is 325 K, for a moderate exciton density not exceeding $(10a_B)^{-2}$ in any one QW. The density dependence of polariton BEC is plotted in

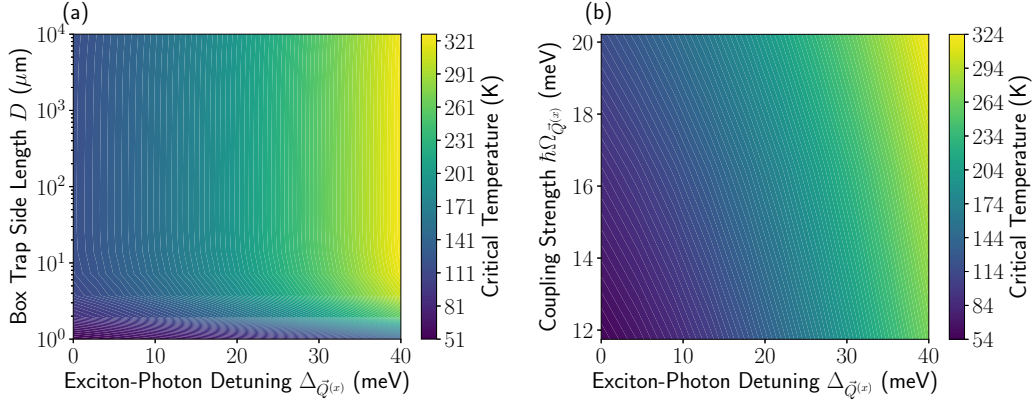


FIG. 11. (a) T_c (represented by the color scale) as functions of the detuning $\Delta_{\tilde{Q}(\alpha)}$ and the trapping size D in a symmetric-woodpile system. Once again, we remind the reader that the sign convention for the detuning is opposite of that traditionally found in the literature. The QW width is 2 nm, while the barrier layer width is 4 nm. The exciton-photon coupling is $\hbar\Omega_{\tilde{Q}(\alpha)} = 20$ meV for three QWs in the central slab. The PhC lattice constant is $264 \leq a \leq 270$ nm. The exciton recombination energy is 1.966 eV. The polariton density is $(10a_B)^{-2}/\max(P_i)$. (b) T_c (color scale) as functions of the exciton-photon coupling $\hbar\Omega_{\tilde{Q}(\alpha)}$ and the detuning $\Delta_{\tilde{Q}(\alpha)}$ for $D = 10 \mu\text{m}$. The QW width is still 2 nm, while the barrier layer width is increased to vary the exciton-photon coupling strength (by reducing the number of QWs from three to one). Other parameters are the same as in (a).

Fig. 12. As seen in Ref. [28], the dependence of T_c on D is significant for lower polariton densities. In this regime, both temperature and density are low. Polaritons are thus mainly populated in the states close to the dispersion minima where the effects of excitonlike states are negligible. In this regime, the dependence of T_c on trapping size resembles that of atomic BEC [33]. However, in the high polariton density regime, T_c varies very weakly with D and is mainly limited by the dispersion depth V [28]. Figures 12(b) and 12(c) reveal that high transition temperature is attainable at strong exciton-photon coupling, large detuning, and high polariton density.

B. Symmetry-breaking architectures

We now examine the possibility of room-temperature BEC using slanted-pore crystals or asymmetric-woodpile crystals in which the X-Y polarization degeneracy is broken. These

structures provide a physical realization of the asymmetric polariton dispersions discussed in Sec. III. The structures are composed of AlGaAs ($\epsilon = 9.54$), surrounding a central slab containing two or three AlGaAs/GaAs QWs. The critical temperature in both of these asymmetric architectures follows the same trends in coupling strength, trapping size, detuning, and density as shown in the previous subsection.

We depict the slanted-pore structure in Fig. 13(a) and its band structure in Fig. 13(b). The slanted-pore system has the advantage of a larger photonic band gap to central frequency ratio than the symmetric-woodpile structure (15.5% compared to 12.0%) as well as a larger remaining gap between the lowest guided band and the lower three-dimensional band edge (6% compared to 2%). This allows for stronger light localization to the central slab, resulting in larger light-matter coupling strengths to enhance the BEC critical temperature. The broken X-Y symmetry lifts the degeneracy of the two photonic minima

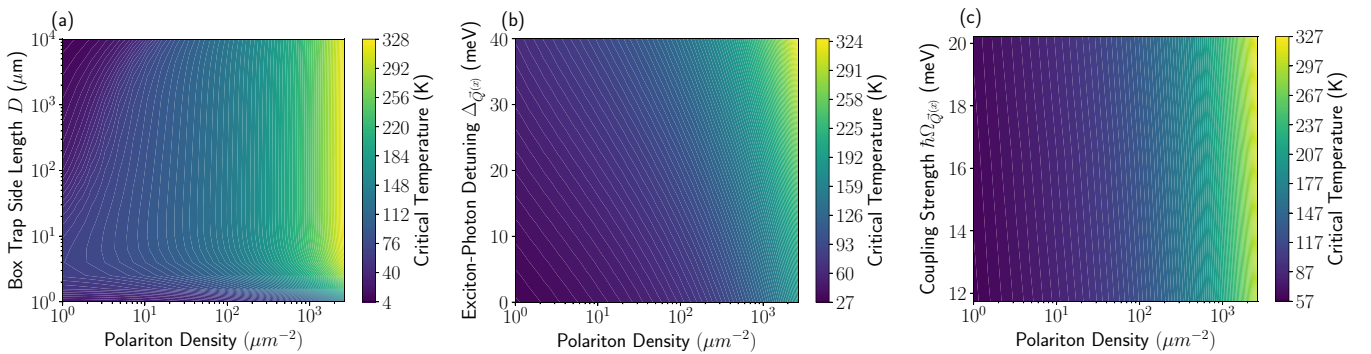


FIG. 12. (a) Polariton BEC transition temperature T_c (represented by the color scale) as a function of the trapping size D and the polariton density. The widths of the GaAs QW and the AlAs barrier layer are 2 nm and 4 nm, respectively. The exciton-photon coupling is $\hbar\Omega_{\tilde{Q}(\alpha)} = 20$ meV for three QWs in the central slab, while the detuning is $\Delta_{\tilde{Q}(\alpha)} = 40$ meV. The PhC lattice constant is 270 nm. The exciton recombination energy is 1.966 eV. (b) T_c (color scale) as a function of the detuning $\Delta_{\tilde{Q}(\alpha)}$ and the polariton density. $D = 10 \mu\text{m}$. The other parameters are the same as in (a). (c) T_c (color scale) as a function of the exciton-photon coupling $\hbar\Omega_{\tilde{Q}(\alpha)}$ and the polariton density. The detuning is $\Delta = 40$ meV, while the trapping size is $D = 10 \mu\text{m}$. The QW width is still 2 nm, while the barrier layer width is increased to modify the exciton-photon coupling strength by reducing the number of QWs. The other parameters are the same as in (a).

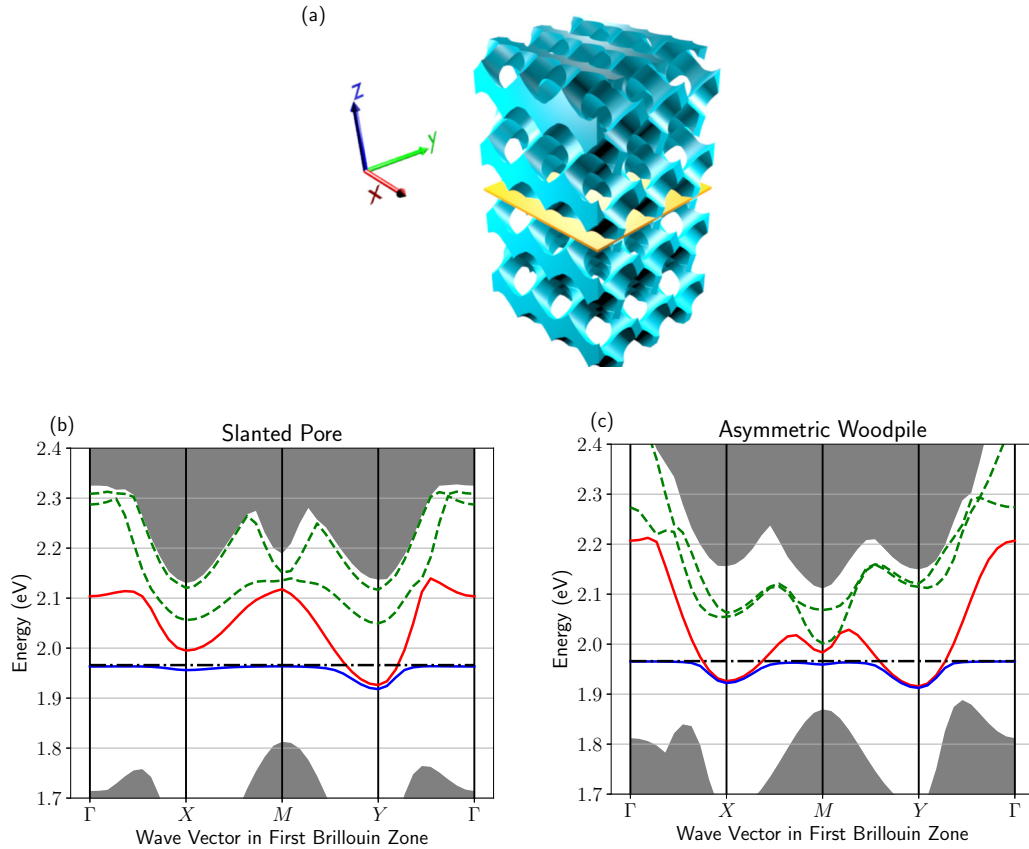


FIG. 13. (a) Schematic of the slanted-pore photonic-crystal cavity. A central slab containing GaAs/AlGaAs QWs is sandwiched in the PhC. (b) Photonic band structure in the 2D Brillouin zone for the slanted pore and (c) asymmetric woodpile with $(h_x, h_y, w_x, w_y) = (0.27a, 0.25a, 0.32a, 0.28a)$. The thicknesses of the central slab layers are $0.08a$ and $0.07a$ in the slanted-pore and asymmetric-woodpile cases, respectively. In (c), the photonic minimum at $\vec{Q}^{(x)}$ is slightly lower by 10.1 meV than that at $\vec{Q}^{(y)}$. The gray (shaded) regions represent the bulk photonic bands. The red (solid) curve in the band gap denotes the lowest confined photonic band. It is placed close to the QW exciton emission line (black [dashed] line) and contributes significantly to the lower polariton branch (blue [solid] curve below the exciton emission line). Other confined photonic bands are represented by the green (dashed) curves. In the slanted-pore system, a lattice constant of $a = 241$ nm is required to obtain exciton-photon detuning $\Delta_{\vec{Q}^{(y)}} = 40$ meV. In the asymmetric-woodpile system, a lattice constant of $a = 269$ nm is needed to obtain exciton-photon detuning $\Delta_{\vec{Q}^{(x)}} = 40$ meV. The light-matter coupling strength is $\hbar\Omega_{\vec{Q}^{(y)}} = 19.8$ meV and $\hbar\Omega_{\vec{Q}^{(x)}} = 13.0$ meV in the slanted-pore and woodpile systems, respectively, for three 2 nm GaAs QWs with 4 nm AlGaAs barriers in the central slab.

at $\vec{Q}^{(x)}$ and $\vec{Q}^{(y)}$, providing a small advantage in T_c and a large advantage in condensate fraction f below T_c .

The asymmetric-woodpile is similar to the symmetric-woodpile crystal, except that the heights and widths of the x - and y -oriented logs (h_x, h_y, w_x, w_y) are not equal. Since we consider the case in which w_x and w_y as well as h_x and h_y differ by only about 20 nm, the structure visually appears nearly identical to the one in Fig. 1(a). We present the band structure for the asymmetric-woodpile system below in Fig. 13(c) for a structure in which $(h_x, h_y, w_x, w_y) = (0.28a, 0.28a, 0.25a, 0.27a)$ where $a = 275$ nm. As in the slanted-pore crystal, this broken symmetry lifts the degeneracy of the two photonic minima and results in larger critical temperatures. The asymmetric structure has one slight disadvantage of a smaller 3D photonic band gap than its symmetric counterpart (10.6% compared to 12.0%) as well as a smaller remaining band gap (1.7% compared to 2.0%). This makes the polaritons more susceptible to radiative decay in the presence of structural disorder (see Sec. VI).

In Fig. 14, we plot the dependence of the light-matter coupling strength, the lattice constant (for detuning fixed

at $\Delta_{\vec{Q}^{(y)}} = 40$ meV), and the critical temperature on the quantum well width. In Fig. 14(a), we remark that the coupling strengths of the slanted-pore system are smaller than that in the symmetric-woodpile system. Though the slanted-pore system has a larger band gap, it requires a thicker central slab than in either of the woodpile systems ($0.08a$ compared to $0.07a$) to accommodate three QWs. This is due to the fact that for a given exciton-photon detuning $\Delta_{\vec{Q}^{(y)}}$, the lattice constant is smaller in the slanted-pore system than in either of the woodpile systems, as shown in Fig. 14 for the case of $\Delta_{\vec{Q}^{(y)}} = 40$ meV. As a result of the thicker central slab, there is a larger confinement volume in the slanted-pore system and a slightly weaker field intensity (see Appendix D). We attribute the slightly weaker coupling strength in the asymmetric woodpile system to reduced PBG and light localization relative to the symmetric woodpile (see Appendix D). Figure 14(c) reveals that both the asymmetric-woodpile and the slanted-pore systems outperform the symmetric woodpile in terms of critical temperature. We attribute this slight improvement to (i) symmetry breaking and (ii) slightly weaker coupling strengths, which yields slightly more photonlike polaritons that in turn

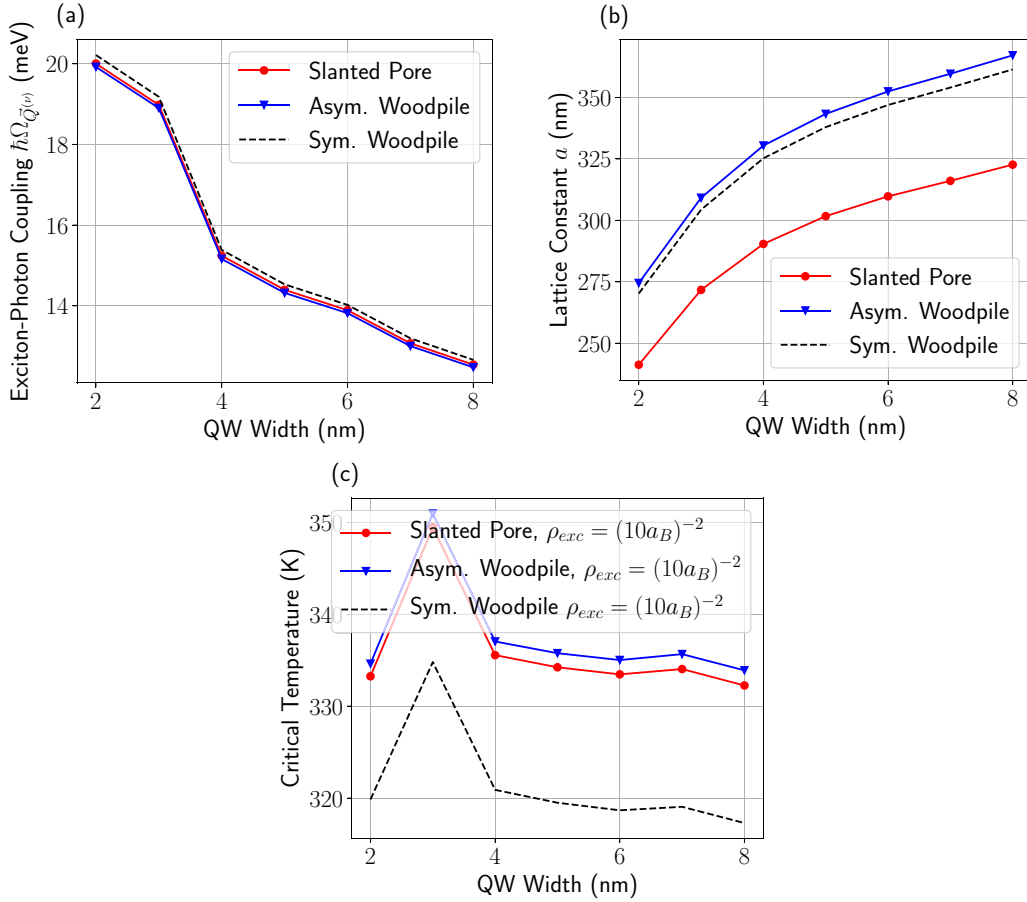


FIG. 14. (a) Collective exciton-photon coupling $\hbar\Omega_{\tilde{Q}^{(x)}}$ as a function of the QW width for AlGaAs slanted-pore and asymmetric and symmetric woodpile PhC cavities. The coupling is evaluated at $\tilde{Q}^{(x)}$ and $\tilde{Q}^{(y)}$ for the woodpile-based and slanted-pore systems, respectively. The central slab is $0.07a$ and $0.08a$ thick in the woodpile and slanted-pore cases, and each contain three QWs. The width of the AlAs barrier layers here is fixed at 4 nm. The interband dipole matrix element is $d = 1.1 \times 10^{-28}$ C m. (b) The in-plane PhC lattice constant a as a function of QW width for the PhC microcavities. The lattice constant varies so as to maintain a fixed detuning of $\Delta_{\tilde{Q}^{(x)}} = 40$ meV. (c) QW width dependence of the polariton BEC transition temperature T_c for polariton density $(10a_B)^{-2}/\max(P_I)$ in the asymmetric and symmetric woodpile, as well as the slanted-pore architectures. The cavity is taken to be a square quantum box of length $D = 10 \mu\text{m}$. The detuning is $\Delta_{\tilde{Q}^{(x)}} = 40$ meV for all QW widths. The exciton-photon coupling strength is given in (a), while the PhC lattice constant is given in (b).

facilitates larger polariton densities. Figure 15 depicts the detuning and exciton density dependence of the critical temperatures for all three structures. As expected, with increasing detuning and density, the critical temperature increases in all three architectures. A roughly 15 K improvement in the BEC critical temperature [at $\Delta_{\tilde{Q}^{(x)}} = 40$ meV and exciton density $\rho_{exc} = (10a_B)^{-2}$] is seen for the asymmetric structures relative to the symmetric one, considering the Penrose-Onsager criterion. This increase in T_c due to asymmetry is larger than that predicted by the toy model in Sec. III, since the densities considered here are higher. In Fig. 8, the maximum polariton density is $(5a_B)^{-2}$, while in Fig. 15, polariton densities are up to $(2.2a_B)^{-2}$ [at an exciton density of $(10a_B)^{-2}$].

VI. DISORDER EFFECTS ON MICROCAVITY POLARITONS

In this section we discuss the effects of disorder on microcavity polaritons. In PhC microcavities disorder can arise from

several sources: (i) the geometric imperfections of the PhC microcavity that mainly affect the photonic spectrum, (ii) the electronic disorder due to impurities, local potentials, strains, QW width, spatial nonuniformity, interfaces, etc., that give rise to inhomogeneous broadening of the excitonic recombination energy, (iii) dynamic disorder due to, e.g., exciton-phonon and exciton-exciton scattering that homogeneously broadens the excitonic levels.

The effect of geometric imperfections of the PhC cavity can be studied via numerical calculations. A rough way to estimate how much geometric fluctuation is tolerable is to calculate the spectrum of the lowest 2D photonic band for various spatial resolutions. We find that the calculation converges at a spatial resolution of about 6 nm (with relative error smaller than 2%). That is, geometric imperfections below 6 nm have negligible effect on the photonic spectrum and optical field distribution. We further notice that the geometric imperfections around the slab layer are most deleterious. In contrast, geometric imperfections in the cladding layers are more tolerable (can be up to 20 nm).

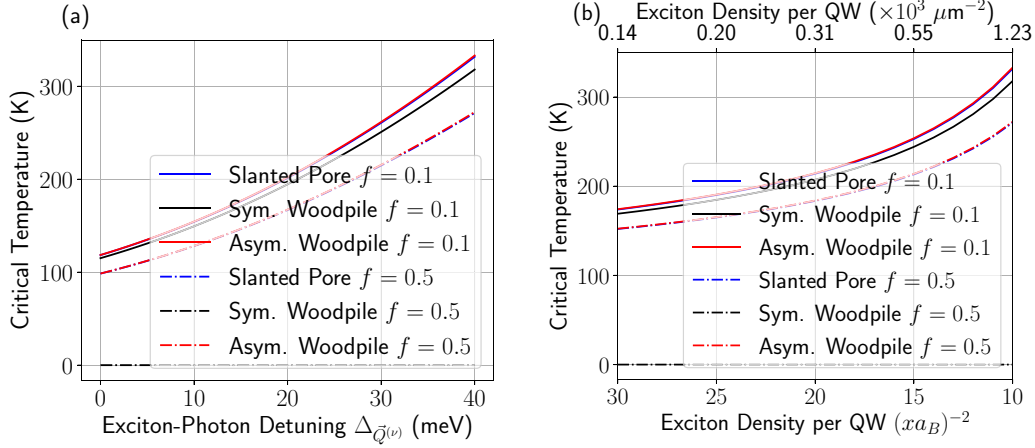


FIG. 15. (a) Critical temperature as a function of exciton-photon detuning $\Delta_{\tilde{Q}^{(\nu)}}$, where $\nu = x$ for both the symmetric and asymmetric woodpile structures and $\nu = y$ for the slanted-pore structure. The polariton density is $(10a_B)^{-2}/\max(P_l)$. (b) Critical temperature as a function of the exciton density per QW. The detuning is $\Delta_{\tilde{Q}^{(\nu)}} = 40$ meV. In both (a) and (b), there are three 2 nm QWs in the central slab, with the coupling strength given by Fig. 14(a). The box trap side length is $D = 10 \mu m$; the exciton recombination energy and Bohr radius are $E_X = 1.966$ eV and $a_B = 9$ nm. The results for T_c are shown for condensate fractions $f = 0.1$ (solid lines) and $f = 0.5$ (dashed lines). In the case of the symmetric woodpile, the critical temperature is identically zero for a condensate fraction of $f = 0.5$.

The effect of electronic disorder for the single QW case has been studied in Ref. [32] where the small polariton effective mass makes them highly mobile and the disorder potential is averaged over a large spatial scale. Consequently, disorder within a QW has little effect, analogously to motional narrowing [32]. In addition to the disorders within one QW, there also exists inhomogeneous broadening of the exciton recombination energy among different QWs. Such inhomogeneous broadening arises from variations in the width of each QW, which changes the exciton recombination energy (cf. Fig. 9). This can be described by adding a fluctuating part to the exciton energy within each QW, i.e., $E_{1s}^{(l)}(\vec{q}) = E_{1s}(\vec{q}) + \delta E_l$ with δE_l describing the random fluctuation. Here δE_l is modeled as a Gaussian random variable with the variance $(\delta E_{1s})^2$. δE_{1s} is referred to as ‘‘inhomogeneous broadening.’’ Reference [63] suggests that the inhomogeneous broadening in GaAs-based QWs may be less than 1 meV due to precise fabrication technologies. Previous work [28,29,36] has shown that the light-matter coupling strength $\hbar\Omega_{\tilde{Q}^{(\nu)}}$, the dispersion depth V , and the critical temperature T_c are robust to inhomogeneous broadening of $\delta E_{1s} \leq 10$ meV in systems with multiple QWs.

The effect of dynamic disorder, such as the polariton-phonon and polariton-polariton scatterings, differs from that of static disorder. Dynamic disorder causes both level broadening and finite lifetime of a polariton state. The latter is crucial for the establishment of thermal equilibrium of the condensate. For GaAs QWs at room temperature the homogeneous broadening is mainly caused by optical phonon scattering, which gives rise to a linewidth of 8 meV [64]. This linewidth gives a phonon scattering time of 0.08 ps. Accordingly, the thermalization time for polaritons is on the order of 1 ps for the ranges of the exciton-photon coupling and detuning studied in this work. The effect of dynamic disorder on polariton dispersion depth can be modeled by adding an imaginary part, $i\Gamma$, to the exciton

energy, which gives

$$V_{\tilde{Q}^{(\nu)}} = \frac{\Delta_{\tilde{Q}^{(\nu)}}}{2} + \text{Re} \sqrt{\left(\frac{\Delta_{\tilde{Q}^{(\nu)}} - i\Gamma}{2}\right)^2 + \hbar^2 \Omega_{\tilde{Q}^{(\nu)}}^2}, \quad (19a)$$

$$V = \max\{V_{\tilde{Q}^{(x)}}, V_{\tilde{Q}^{(y)}}\}. \quad (19b)$$

In general, exciton-phonon interaction reduces the dispersion depth V . However, for $\Delta_{\tilde{Q}^{(x)}} = 40$ meV, $\hbar\Omega_{\tilde{Q}^{(x)}} = 20$ meV, and $\Gamma = 8$ meV, the lower polariton dispersion depth is reduced by only 0.2 meV. This is equivalent to a reduction of detuning by 0.2 meV and has negligible effects on the transition temperature according to Fig. 12(b).

We finally discuss the effect of nonradiative recombination mechanisms on polariton BEC. It is found that the Auger recombination lifetime for the highest density of carriers studied in this work is about 10^{-3} s according to the calculation in Ref. [65], which is negligible. Another mechanism is the Shockley-Read-Hall mechanism [66] of which the decay rate is proportional to the density of defects. This mechanism can be reduced in high-quality samples which can be fabricated with advanced growth technology of photonic-crystal cavities [37,41,42]. Finally the photon lifetime is determined by the quality of the cavity which can be improved by increasing the thickness of the cladding PhCs. In the literature, quality factors as high as 10^6 and photon lifetimes as long as nanoseconds have been achieved in PhC microcavities [37].

VII. CONCLUSIONS AND DISCUSSION

In summary, we have identified a window of opportunity to achieve above-room-temperature polariton BEC in GaAs quantum wells using AlGaAs photonic-band-gap

microcavities. We compared symmetric-woodpile, asymmetric-woodpile, and slanted-pore architectures sandwiching a central slab containing three GaAs/AlAs quantum wells for effective regimes of exciton-photon detuning and polariton density. The full three-dimensional photonic band gap of our structures allows for strong light localization resulting in strong exciton-photon coupling within the central slab. The photonic band gap also inhibits the radiative decay of trapped exciton-polaritons through strongly coupled, off-normal, leaky modes and allows for them to fully thermalize with each other and the host lattice. The coupling strength of the exciton to leaky off-normal modes in a 1D Fabry-Pérot cavity depends sensitively on the Fourier components of the exciton wave function within the trapping region. In contrast, the 3D PBG completely eliminates leaky modes and the polariton lifetime is limited only by exciton nonradiative recombination.

The most sensitive factors enabling high-temperature BEC are the polariton dispersion depth and the polariton density. The former is enhanced by strong exciton-photon coupling and large, positive, exciton-photon detuning. Our calculations suggest that a detuning of 40 meV or more provides the necessary window of opportunity, where the dispersion depth exceeds room temperature and the exciton fraction of the relevant polaritons is sufficiently small to allow a high polariton density. At the same time, the exciton fraction is sufficiently high to allow rapid thermalization of the polariton gas. In our calculations, we found room-temperature BEC while keeping the exciton density below $(10a_B)^{-2}$ per quantum well. Even higher onset temperatures for BEC are likely feasible by slight further increases in detuning and polariton density, without the deleterious effects of excitonic Auger recombination [65].

We introduced a toy model to explain the effect of valley degeneracy in the polaritonic spectrum on BEC critical temperature and condensate fraction. The proximal excitonic density of states was shown to define the critical temperature more than the valley degeneracy. Breaking of X-Y symmetry to lift the valley degeneracy provided a boost of 15 K, at most, in the BEC onset temperature as defined by the Penrose-Onsager criterion. On the other hand, the condensate fraction at lower temperatures is considerably enhanced by symmetry breaking. High condensate fractions at or slightly below room temperature may be very important in exploring novel quantum many-body states and fragmented condensates [59] in the presence of moderate exciton-exciton interactions.

Considerable challenges still exist in realizing large-scale 3D photonic-band-gap materials with a large PBG in the visible spectrum. In the present optical microcavity, only four unit cells of photonic crystal above and below the central slab containing three quantum wells is required. Such photonic crystals can initially be defined in polymer templates and then transferred to high-index semiconductors [43]. More recently, it has been shown [67] that III-V semiconductors can be epitaxially grown through a suitable template structure to achieve a 3D photonic band gap material with high electronic quality. Such a technique could be used to realize the 3D PBG claddings of AlGaAs considered in this paper. Another suitable material for our PBG microcavity is GaP, which is nonabsorbing in the energy range of our quantum well exciton-polariton and has a dielectric constant of 11.11 [68]. The

TABLE II. Material parameters for the calculation of QW exciton states. All the parameters are taken from Ref. [51]. The conduction band effective mass of AlAs is determined by fitting the excitonic absorption energy in Ref. [8]. The static dielectric constant is taken from Ref. [50]. The dielectric constant at optical frequency is taken from Ref. [69]. The parameters γ_1, γ_2 , and γ_3 describe the effective mass anisotropy for the $J = \frac{3}{2}$ holes in GaAs.

	m_e/m_0	γ_1	γ_2	γ_3	ϵ (static)	ϵ (optical)
GaAs	0.065	6.98	2.06	2.93	12.8	12.5
AlAs	0.06	3.76	0.82	1.42		8.8

ingredients required for the fabrication of our desired 3D PBG microcavity are available. It is hoped that the important outcomes of long-lived, equilibrium Bose condensates and other mesoscopic quantum superposition states at room temperature will strongly motivate the needed fabrication efforts [70–79].

ACKNOWLEDGMENTS

We thank Hui Deng, Shengjun Yang, Wah-Tung Lau, and David Hagenmüller for helpful discussions. This work was supported by the Natural Sciences and Engineering Research Council of Canada, the Canadian Institute for Advanced Research, and the United States Department of Energy Contract No. DE-FG02-06ER46347.

APPENDIX A: CALCULATION OF THE CONFINED PHOTONIC BANDS

The dispersion and field distribution of the confined photonic bands are calculated via the plane wave expansion method [46]. The dielectric constants at optical frequency of GaAs and AlAs are listed in Table II. The woodpile rods constituting the 3D PBG cladding are made up of $\text{Al}_{0.8}\text{Ga}_{0.2}\text{As}$ with dielectric constant given by the linear interpolation between that of GaAs and AlAs, i.e., $\epsilon(\text{Al}_{0.8}\text{Ga}_{0.2}\text{As}) = 0.8\epsilon(\text{AlAs}) + 0.2\epsilon(\text{GaAs}) = 9.54$. For the central slab, the dielectric constant is simply taken as the average $0.5\epsilon(\text{AlAs}) + 0.5\epsilon(\text{GaAs}) = 10.7$. The resolution of the calculation is tested to have relative error of about 5% or less. The imaginary part of the dielectric function of $\text{Al}_{0.8}\text{Ga}_{0.2}\text{As}$ is negligible for photon energy below 2.3 eV.

APPENDIX B: EXCITONIC STATES

The lowest energy excitonic state in the QWs is the heavy-hole exciton at $1s$ state. This is so because the first heavy-hole subband has much lower energy than the light-hole one. By separating the relative motion and center-of-mass degrees of freedom, the wave function can be written as

$$|\Psi_{\alpha, \vec{k}}\rangle = \sum_{\vec{q}} \eta_{\vec{q}, \vec{k}} \zeta_{\alpha, \sigma, \sigma'} c_{\vec{k}/2 + \vec{q}, \sigma}^\dagger d_{\vec{k}/2 - \vec{q}, \sigma'}^\dagger |0\rangle, \quad (\text{B1a})$$

$$\eta_{\vec{q}, \vec{k}} = \frac{1}{\sqrt{S}} \int d\vec{\rho}_{\text{eh}} \phi_1(\vec{\rho}_{\text{eh}}) e^{-i[\vec{q} + \frac{m_h - m_e}{m_h + m_e} \frac{\vec{k}}{2}] \cdot \vec{\rho}_{\text{eh}}}. \quad (\text{B1b})$$

S is the area of the system. $\phi_1(\vec{\rho}_{\text{eh}})$ is the wave function of the QW $1s$ hydrogenic state with $\vec{\rho}_{\text{eh}} = \vec{\rho}_e - \vec{\rho}_h$. The above wave function gives an exciton state with center-of-mass

momentum of $\hbar\vec{k}$. The center-of-mass coordinate is $\vec{R} = (m_e\vec{\rho}_e + m_h\vec{\rho}_h)/(m_e + m_h)$ and the center-of-mass wave function is $e^{i\vec{k}\cdot\vec{R}}$. c_σ^\dagger (d_σ^\dagger) creates an electron (heavy-hole) with spin σ . ζ_α gives the internal spin structure of the electron and heavy-hole determined by the polarization $\alpha = L, T$ (longitudinal or transverse polarization). Specifically [49]

$$\zeta_L = \begin{pmatrix} 0 & \frac{1}{\sqrt{2}}e^{i\theta_{\vec{k}}} \\ \frac{-1}{\sqrt{2}}e^{-i\theta_{\vec{k}}} & 0 \end{pmatrix},$$

$$\zeta_T = \begin{pmatrix} 0 & \frac{i}{\sqrt{2}}e^{i\theta_{\vec{k}}} \\ \frac{i}{\sqrt{2}}e^{-i\theta_{\vec{k}}} & 0 \end{pmatrix}, \quad (\text{B2})$$

where $\theta_{\vec{k}} = \text{Arg}(k_x + ik_y)$. The spectrum of the exciton is

$$E_{\text{ps}}(\vec{k}) = E_{\text{ps}} + \frac{\hbar^2 k^2}{2(m_e + m_h)}, \quad (\text{B3})$$

where E_{ps} is the energy of stationary exciton ($\vec{k} = 0$) at the p th s -orbital state.

The single-particle electronic states for the conduction and valence bands are

$$\langle \vec{r} | c_{\vec{q},\sigma}^\dagger | 0 \rangle = \frac{1}{\sqrt{S}} e^{i\vec{q}\cdot\vec{\rho}} u_{\Gamma_c}(\vec{\rho}, z) \xi_c(z) \chi_\sigma, \quad (\text{B4})$$

$$\langle \vec{r} | d_{\vec{q},\sigma}^\dagger | 0 \rangle = \frac{1}{\sqrt{S}} e^{i\vec{q}\cdot\vec{\rho}} u_{\Gamma_v}(\vec{\rho}, z) \xi_v(z) \chi_\sigma, \quad (\text{B5})$$

respectively. u_{Γ_c} and u_{Γ_v} are the Bloch wave function for the electronic conduction and valence bands at the Γ point, respectively. ξ_c (ξ_v) is the wave function of the lowest subband in the conduction (valence) band. χ_σ denotes the spin state of the electron or hole.

To study the system we calculate the QW excitonic states from effective mass approximation using realistic parameters. First the the electron and hole subband states in the QW are calculated with the position-dependent effective mass model [48]

$$H_{\text{sub}} = \hat{P}_z \frac{1}{2m(z)} \hat{P}_z + V(z), \quad (\text{B6})$$

with $\hat{P}_z = -i\hbar\partial_z$. The treatment in this part will follow the standard method in Ref. [48]. The electron effective mass in the GaAs QW and AlAs barrier layer as well as the Luttinger parameters [49,54] for the valence bands are taken from Ref. [51] and listed in Table II where m_0 is the bare electron mass in vacuum. The ratio of conduction band edge offset to the whole band gap difference at the Γ point between GaAs and AlAs is taken as 66% [51]. The band gap of GaAs at room temperature is 1.424 eV whereas at very low (e.g., 4 K) temperature it is 1.519 eV [50,51]. Therefore the conduction (valence) band offset of the QW is 1 eV (0.52 eV) at room temperature [50,51]. For 4 K the conduction band offset is 1.04 eV, while the valence band offset is 0.54 eV.

For heavy holes in [001] QWs the effective mass along the z direction is given by [49,80]

$$\frac{m_{\text{hhz}}}{m_0} = \frac{1}{\gamma_1 - 2\gamma_2}, \quad (\text{B7})$$

whereas for light holes it is

$$\frac{m_{\text{lh}z}}{m_0} = \frac{1}{\gamma_1 + 2\gamma_2}. \quad (\text{B8})$$

The effective mass relevant for the motion in the QW plane is obtained via the following average:

$$\frac{1}{m_e} = \frac{p_{\text{QW}}}{m_e(\text{GaAs})} + \frac{1 - p_{\text{QW}}}{m_e(\text{AlAs})}, \quad (\text{B9})$$

$$\frac{1}{m_h} = \frac{p_{\text{QW}}}{m_{\text{hh}\parallel}(\text{GaAs})} + \frac{1 - p_{\text{QW}}}{m_{\text{hh}\parallel}(\text{AlAs})} + \frac{1}{m'_h} \quad (\text{B10})$$

with $p_{\text{QW}} = \int dz |\xi_{c/v}(z)|^2|_{z \in \text{QW}}$ being the probability of electron (or hole) in the GaAs QW region. Here m'_h is the correction due to inter-subband heavy-hole–light-hole mixing and

$$\frac{m_{\text{hh}\parallel}}{m_0} = \frac{1}{\gamma_1 + \gamma_2}. \quad (\text{B11})$$

The contribution from the mixing of heavy and light holes comes from the off-diagonal term in the Luttinger Hamiltonian [49,54], $\pm\sqrt{3}\frac{\hbar}{m_0}\gamma_3(k_x \pm ik_y)\hat{P}_z$ [49]. Second-order perturbation theory yields an energy correction which is proportional to $|\vec{k}|^2$ and thus contributes to the heavy-hole effective mass. This contribution is written as [49]

$$\frac{1}{m'_h} = -\frac{3}{8} \sum_n \frac{|\langle \text{hh}, 1 | \hat{P}_z \gamma_3(z) + \gamma_3(z) \hat{P}_z | \text{lh}, n \rangle|^2}{m_0^2(E_{\text{lh},n} - E_{\text{hh},1})}, \quad (\text{B12})$$

where $|\text{hh}, 1\rangle$ is the first heavy-hole subband and $|\text{lh}, n\rangle$ is the n th light-hole subband with their energy being $E_{\text{hh},1}$ and $E_{\text{lh},n}$, respectively. For narrow QWs the main contribution of this correction comes from the mixing between the first heavy-hole subband and the second light-hole subband. Other valence band mixing terms in the Luttinger Hamiltonian [54] induce nonparabolic effect in the heavy-hole subband. Broido and Sham have shown that such corrections affect the properties of the heavy-hole exciton marginally [53]. We hence ignore those corrections in this work.

For narrow QWs of which the subband splitting is much larger than the Coulomb interaction, the exciton Hamiltonian can be reduced to the single subband form

$$H_{\text{ex}} = -\frac{\hbar^2 \partial_{\vec{\rho}_e}^2}{2m_e} - \frac{\hbar^2 \partial_{\vec{\rho}_h}^2}{2m_h} + V_{\text{QW}}(\vec{\rho}_e - \vec{\rho}_h), \quad (\text{B13})$$

where the Coulomb potential in the lowest subband is

$$V_{\text{QW}}(\vec{\rho}_e - \vec{\rho}_h) = - \int \frac{dz_e dz_h e^2 |\xi_c(z_e)|^2 |\xi_v(z_h)|^2}{4\pi \epsilon_0 \epsilon \sqrt{(\vec{\rho}_e - \vec{\rho}_h)^2 + (z_e - z_h)^2}}.$$

Since the electrons/holes mainly stay in the GaAs QW region, we ignore the difference between the static dielectric constant of GaAs and that of AlAs for simplicity. The excitonic states and spectra are calculated numerically by exactly diagonalization of the above Hamiltonian. The most efficient method is to use the 2D excitonic states as basis states. The width of the AlAs barrier layer between GaAs QWs is set to be sufficiently large so that tunneling of electrons and holes between QWs is negligible. Specifically the tunneling-induced subband energy shift is less than 1 meV and the wave function penetration is less than 1%. With the parameters in Table II, we

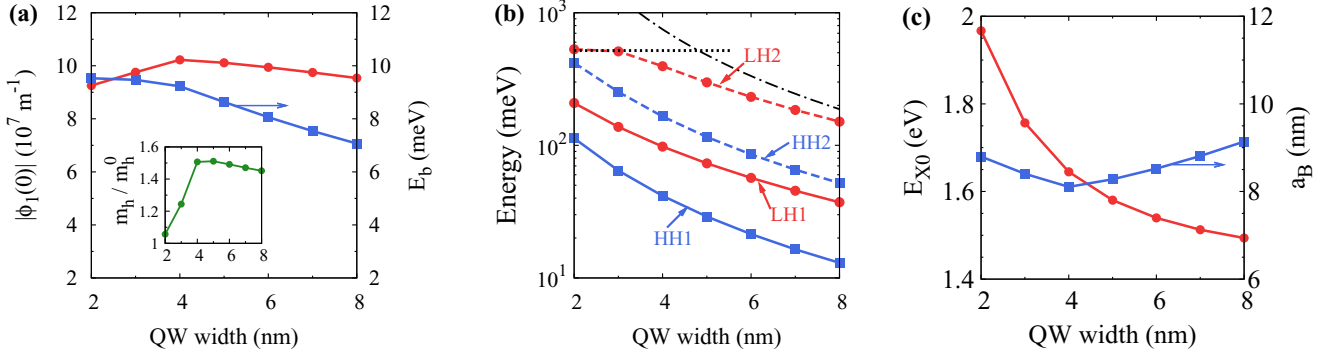


FIG. 16. (a) QW width dependencies of the QW exciton wave function at zero electron-hole distance $|\phi_1(0)|$ and the exciton binding energy E_b . Inset: hole effective mass m_h/m_h^0 with $m_h^0 = m_0/(\gamma_1 + \gamma_2)$ (γ_1 and γ_2 here are the Luttinger parameters [54] of GaAs). (b) The subband edges as functions of the QW width. “HH1” and “HH2” denote the first and second heavy-hole subbands, while “LH1” and “LH2” stand for the first and second light-hole subbands. The chained curve represents a l_{QW}^{-2} (l_{QW} denoting the QW width) dependence. The dotted line marks the barrier height for holes of the GaAs/AlAs QW. (c) The exciton recombination energy E_{1s} and Bohr radius a_B as functions of QW width. The width of AlAs barrier between QWs is taken as 4 nm.

are able to reproduce the exciton absorption energy in Ref. [8]. We note there are two types of excitons, longitudinal and transverse. The spectra of the two are generally not degenerate due to (i) the long-range exchange splitting due to the coupling with photon and (ii) the short-range exchange splitting due to interband Coulomb interaction. Mechanism (i) is in fact the polaritonic effect we consider in this work, whereas (ii) is negligible for [001]-grown GaAs QWs. We thus use the same dispersion for both types of excitons.

The excitonic wave function at zero electron-hole relative distance $|\phi_1(0)|$ can be obtained directly via the ground state wave function from exact diagonalization. As the ground-state wave function $\phi_1(\vec{\rho}_{\text{eh}})$ is no longer exactly exponential we define the exciton Bohr radius as

$$a_B \equiv \left[2\pi \int d\vec{\rho}_{\text{eh}} |\phi_1(\vec{\rho}_{\text{eh}})|^4 \right]^{-\frac{1}{2}}. \quad (\text{B14})$$

Inserting the 2D excitonic wave function into the above definition yields the standard result

$$a_B = \frac{1}{2} a_0 \frac{\varepsilon m_0}{m_{\text{red}}}, \quad (\text{B15})$$

where the hydrogen Bohr radius $a_0 = 0.53 \text{ \AA}$, ε is the static dielectric constant, and the reduced mass $m_{\text{red}} = \frac{m_e m_h}{m_e + m_h}$.

Figure 16(a) shows the exciton wave function at zero electron-hole relative distance $|\phi_1(0)|$ and the exciton binding energy E_b as a function of QW width. The exciton binding energy is defined as the energy difference between the semiconductor band gap and the exciton ground-state energy E_{1s} . It is noticed that $|\phi_1(0)|$ has a nonmonotonic dependence although E_b is still monotonic. This is due to a nonmonotonic dependence of the effective mass of the lowest heavy-hole subband m_h as shown in the inset. The latter originates from the correction m'_h . It has a peak when the wave function of the second light-hole subband starts to spread considerably outside the QW into the barrier. From Fig. 16(b) it is seen that the QW width l_{QW} dependence of the second light-hole subband edge deviates significantly from the l_{QW}^{-2} around $l_{\text{QW}} = 4 \text{ nm}$ and saturates at the barrier height for the valence band in the GaAs/AlAs QW, 0.52 eV [50,51], as indicated by the dotted

line in the figure. This signals that the wave function of the second light-hole subband becomes largely unconfined to the QW. As the second light-hole subband becomes gradually deconfined its mixing with the first heavy-hole subband is considerably reduced. Since m'_h is negative, this results in a reduction of m_h . Consequently the Bohr radius increases [see Fig. 16(c)] and $|\phi_1(0)|$ decreases. For completeness we also plot the exciton recombination energy E_{1s} and the exciton Bohr radius a_B as functions of the QW width in Fig. 16(c).

To determine the interband dipole matrix element, we calculate the exciton-photon coupling in the FP microcavity and compare it with the experimental measurements in Ref. [8]. The confined photonic mode in the FP microcavity is calculated via the finite difference time domain method. The energy and field distribution of the confined photonic band is then utilized to obtain the exciton-photon coupling and fitted to the measured VRS in Ref. [8]. The only fitting parameter is the interband dipole matrix element d , or equivalently the energy E_{cv} through

$$d = \frac{e\hbar\sqrt{E_{\text{cv}}}}{E_g\sqrt{2m_0}}. \quad (\text{B16})$$

Here $E_{\text{cv}} = 2P_{\text{cv}}^2/m_0$ is related to the momentum matrix element between the conduction and valence bands P_{cv} . The fitted value is $E_{\text{cv}} = 24 \text{ eV}$ which is slightly smaller than the widely accepted value of 25.5–29 eV [51]. From the fitted value of E_{cv} the interband dipole matrix element is determined as $d = 1.1 \times 10^{-28} \text{ C m}$ which is used throughout this work.

APPENDIX C: EXCITON-PHOTON COUPLING

1. Exciton-photon coupling: Single quantum well

The Hamiltonian of exciton-photon coupling is written as

$$H = e\vec{r} \cdot \vec{\mathcal{E}}(\vec{r}), \quad (\text{C1})$$

where $e > 0$ is the elementary charge and the electric field of the quantized photon is

$$\vec{\mathcal{E}}(\vec{r}) = i \sum_{\vec{q}} \sqrt{\frac{\hbar\omega_{\vec{q}}}{2\varepsilon_0 S}} \vec{u}_{\vec{q}}(\vec{\rho}, z) e^{i\vec{q} \cdot \vec{\rho}} a_{\vec{q}} + \text{H.c.} \quad (\text{C2})$$

The exciton-photon coupling in the rotating wave approximation is then written as

$$H_{\text{int}} = \sum_{\alpha, \vec{k}, \vec{q}} i \hbar \Omega_{\alpha, \vec{k}, \vec{q}} \beta_{\alpha, \vec{k}}^{\dagger} a_{\vec{q}} + \text{H.c.}, \quad (\text{C3})$$

$$\hbar \Omega_{\alpha, \vec{k}, \vec{q}} = \sqrt{\frac{\hbar \omega_{\vec{q}}}{2 \varepsilon_0 S}} \langle \Psi_{\alpha, \vec{k}} | \vec{u}_{\vec{q}}(\vec{\rho}, z) e^{i \vec{q} \cdot \vec{\rho}} \cdot e \vec{r} | 0 \rangle \quad (\text{C4})$$

$$= \sqrt{\frac{\hbar \omega_{\vec{q}}}{2 \varepsilon_0 S}} \tilde{\Omega}_{\alpha, \vec{k}, \vec{q}}, \quad (\text{C5})$$

where β^{\dagger} and a^{\dagger} are the creation operators of exciton and photon, respectively. Inserting the exciton wave function $|\Psi_{\alpha, \vec{k}}\rangle$ from Eq. (B1b) we find

$$\tilde{\Omega}_{\alpha, \vec{k}, \vec{q}} = \sum_{\vec{k}'} \eta_{\vec{k}', \vec{k}} d_{\alpha} \int h_{\alpha, \vec{k}, \vec{q}}(\vec{\rho}, z) d \vec{\rho} dz, \quad (\text{C6})$$

with d_{α} being the magnitude of the dipole of the α -polarized exciton. Here

$$h_{\alpha, \vec{k}, \vec{q}}(\vec{\rho}, z) = S^{-1} \xi_c^*(z) e^{i(\vec{q}-\vec{k}) \cdot \vec{\rho}} u_{\alpha, \vec{q}}(\vec{\rho}, z) \xi_v(z), \quad (\text{C7})$$

where $u_{\alpha, \vec{q}} = \vec{e}_{\alpha} \cdot \vec{u}_{\vec{q}}$ with \vec{e}_{α} being the polarization direction of the α exciton. For the transverse exciton, $\vec{e}_T = \vec{e}_z \times \vec{q}/q$, while for the longitudinal exciton, $\vec{e}_L = \vec{q}/q$. We then find

$$\int d \vec{\rho} dz h_{\alpha, \vec{k}, \vec{q}}(\vec{\rho}, z) \simeq \int d \vec{\rho} S^{-1} e^{i(\vec{q}-\vec{k}) \cdot \vec{\rho}} u_{\alpha, \vec{q}}(\vec{\rho}, z_0) g_{\text{cv}}, \quad (\text{C8})$$

where we have used the approximation

$$\int \xi_c^*(z) \xi_v(z) u_{\alpha, \vec{q}}(\vec{\rho}, z) dz \simeq u_{\alpha, \vec{q}}(\vec{\rho}, z_0) g_{\text{cv}} \quad (\text{C9})$$

with z_0 being the coordinate of the center of the QW along the z direction and

$$g_{\text{cv}} = \int dz \xi_c^*(z) \xi_v(z). \quad (\text{C10})$$

The above approximation is justified when the electromagnetic field varies negligibly over the spatial extent of the QW in the z direction. $|g_{\text{cv}}|$ is very close to unity for the parameters chosen in this work. Hence

$$\tilde{\Omega}_{\alpha, \vec{k}, \vec{q}} \simeq \sum_{\vec{k}'n} \eta_{\vec{k}', \vec{k}} \delta_{\vec{k}, \vec{q} + \vec{G}_n} d_{\alpha} u_{\alpha, \vec{q}, \vec{G}_n}(z_0) g_{\text{cv}}. \quad (\text{C11})$$

Using $\sum_{\vec{k}} \eta_{\vec{k}, \vec{k}} = |\phi_1(0)| \sqrt{S}$, we find

$$\tilde{\Omega}_{\alpha, \vec{k}, \vec{q}} \simeq |\phi_1(0)| \sqrt{S} \sum_n \delta_{\vec{k}, \vec{q} + \vec{G}_n} d_{\alpha} u_{\alpha, \vec{q}, \vec{G}_n}(z_0) g_{\text{cv}}. \quad (\text{C12})$$

We write the Hamiltonian of the exciton-photon system as

$$H = H_X + H_P + H_{\text{int}}, \quad (\text{C13a})$$

$$H_X = \sum_{\alpha \vec{k}} E_{1s}(\vec{k}) \beta_{\alpha, \vec{k}}^{\dagger} \beta_{\alpha, \vec{k}}, \quad (\text{C13b})$$

$$H_P = \sum_{\vec{q}} \hbar \omega_{\vec{q}} a_{\vec{q}}^{\dagger} a_{\vec{q}}, \quad (\text{C13c})$$

$$H_{\text{int}} = \sum_{n, \alpha, \vec{q}} i \hbar \bar{\Omega}_{\alpha, n, \vec{q}} \beta_{\alpha, \vec{q} + \vec{G}_n}^{\dagger} a_{\vec{q}} + \text{H.c.}, \quad (\text{C13d})$$

where β^{\dagger} is the exciton creation operator and

$$\hbar \bar{\Omega}_{\alpha, n, \vec{q}} = |\phi_1(0)| d_{\alpha} u_{\alpha, \vec{q}, \vec{G}_n}(z_0) g_{\text{cv}} \sqrt{\hbar \omega_{\vec{q}} / 2 \varepsilon_0}. \quad (\text{C14})$$

The above model resembles the Dickle model where a single photonic mode couples to many atoms coherently. The collective exciton-photon coupling strength is then written as

$$\hbar \Omega_{\vec{q}} = |\phi_1(0)| |g_{\text{cv}}| \sqrt{\hbar \omega_{\vec{q}} / 2 \varepsilon_0} \left[\sum_{n\alpha} d_{\alpha}^2 |u_{\alpha, \vec{q}, \vec{G}_n}(z_0)|^2 \right]^{1/2} \quad (\text{C15})$$

$$\simeq \hbar \Omega_X \left[\lambda_X \frac{\hbar \omega_{\vec{q}}}{E_{1s}} \sum_{n\alpha} |u_{\alpha, \vec{q}, \vec{G}_n}(z_0)|^2 \right]^{1/2}, \quad (\text{C16})$$

where we have used $|g_{\text{cv}}| \simeq 1$ and $d_{\alpha} \simeq d$ and

$$\hbar \Omega_X \equiv |\phi_1(0)| d \sqrt{E_{1s} / 2 \varepsilon_0 \lambda_X} \quad (\text{C17})$$

with $\lambda_X = hc / E_{1s}$. Here, $\hbar \Omega_X$ serves as a natural unit of the exciton-photon coupling in a semiconductor. From Fourier transformation, we find

$$\sum_n |u_{\alpha, \vec{q}, \vec{G}_n}(z_0)|^2 = S_{\text{uc}}^{-1} \int_{\text{uc}} d \vec{\rho} |u_{\alpha, \vec{q}}(\vec{\rho}, z_0)|^2, \quad (\text{C18})$$

where the integration is performed in the unit cell of the PhC in the x - y plane. Thus

$$\hbar \Omega_{\vec{q}} = \hbar \Omega_X \left[\lambda_X \frac{\hbar \omega_{\vec{q}}}{E_{1s}} S_{\text{uc}}^{-1} \int_{\text{uc}} d \vec{\rho} \sum_{\alpha} |u_{\alpha, \vec{q}}(\vec{\rho}, z_0)|^2 \right]^{1/2}. \quad (\text{C19})$$

Since the magnitudes of the photonic wave vector \vec{G}_n are much smaller than the excitonic wave vector, one can use the approximation $E_{1s}(\vec{k} + \vec{G}_n) \simeq E_{1s}(\vec{k})$. The spectrum of the lower branch polariton is then

$$E_{\text{LP}}(\vec{q}) = \frac{1}{2} (E_{1s}(\vec{q}) + \hbar \omega_{\vec{q}} - \{ [E_{1s}(\vec{q}) - \hbar \omega_{\vec{q}}]^2 + 4 \hbar^2 \Omega_{\vec{q}}^2 \}^{1/2}). \quad (\text{C20})$$

The above spectra can be generated by the following effective Hamiltonian:

$$H = H_0 + H_I, \quad (\text{C21a})$$

$$H_0 = \sum_{\vec{q}} [E_{1s}(\vec{q}) b_{\vec{q}}^{\dagger} b_{\vec{q}} + \hbar \omega_{\vec{q}} a_{\vec{q}}^{\dagger} a_{\vec{q}}], \quad (\text{C21b})$$

$$H_I = \sum_{\vec{q}} i \hbar \Omega_{\vec{q}} (b_{\vec{q}}^{\dagger} a_{\vec{q}} - a_{\vec{q}}^{\dagger} b_{\vec{q}}), \quad (\text{C21c})$$

with

$$b_{\vec{q}} \equiv \sum_{\alpha n} \frac{\bar{\Omega}_{\alpha n \vec{q}}}{\Omega_{\vec{q}}} \beta_{\alpha, \vec{q} + \vec{G}_n} \quad (\text{C22})$$

being the collective exciton operator.

2. Exciton-photon coupling: Multiple quantum wells

We now extend the above derivations to the situations with MQWs. The wave functions of electron and hole in the l th QW

are now written as

$$\begin{aligned} \langle \vec{r} | c_{\vec{q},l,\sigma}^\dagger | 0 \rangle &= \frac{1}{\sqrt{S_e(z_l)}} e^{i\vec{q}\cdot\vec{\rho}} \Theta(\vec{\rho}, z_l) u_{\Gamma_c}(\vec{\rho}, z) \xi_c(z) \chi_\sigma, \\ \langle \vec{r} | d_{\vec{q},l,\sigma}^\dagger | 0 \rangle &= \frac{1}{\sqrt{S_e(z_l)}} e^{i\vec{q}\cdot\vec{\rho}} \Theta(\vec{\rho}, z_l) u_{\Gamma_v}(\vec{\rho}, z) \xi_v(z) \chi_\sigma. \end{aligned}$$

Here $\Theta(\vec{\rho}, z_l)$ is 0 (or 1) in the air (or semiconductor) region and $S_e(z_l)$ is the area of the semiconductor region in the x - y plane for the l th QW. In the case where all QWs are contained in the central slab and none are in the PBG cladding regions, we can set $S_e(z_l) = S$ and $\Theta(\vec{\rho}, z_l) = 1$ for all l . A more detailed account of the scenario in which QWs are placed in the PBG cladding is provided in Refs. [28,29,36]. z_l is the z coordinate at the center of the l th QW. Using the above wave functions and repeating the derivation in the previous section, we obtain the collective exciton-photon coupling:

$$\hbar\Omega = \hbar\Omega_X Y_{\text{cav}}, \quad (\text{C23a})$$

$$Y_{\text{cav}} = \left[\sum_{l,\alpha} \frac{\hbar\omega_{\vec{q}} \lambda_X}{E_{1s}} S_{\text{uc}}^{-1} \int_{\text{uc}} d\vec{\rho} |u_{\alpha,\vec{q}}(\vec{\rho}, z_l)|^2 \Theta(\vec{\rho}, z_l) \right]^{\frac{1}{2}}. \quad (\text{C23b})$$

The dimensionless quantity Y_{cav} characterizes the exciton-photon coupling in the microcavity. Similarly to Eqs. (C21) and (C22), we define the collective exciton operator

$$b_{\vec{q}} \equiv \sum_{l,\alpha n} \frac{\overline{\Omega}_{l,\alpha n \vec{q}}}{\Omega_{\vec{q}}} \beta_{l,\alpha \vec{q} + \vec{G}_n}, \quad (\text{C24})$$

where

$$\begin{aligned} \overline{\Omega}_{l,\alpha n \vec{q}} &= d |\phi_1(0)| \tilde{u}_{\alpha \vec{q}, \vec{G}_n}(z_l) \sqrt{\omega_{\vec{q}} / (2\hbar\epsilon_0)}, \\ \tilde{u}_{\alpha \vec{q}, \vec{G}_n}(z_l) &= S_{\text{uc}}^{-1} \int_{\text{uc}} d\vec{\rho} e^{-i\vec{G}_n \cdot \vec{\rho}} u_{\alpha, \vec{q}}(\vec{\rho}, z_l) \Theta(\vec{\rho}, z_l). \end{aligned} \quad (\text{C25})$$

From Fourier transformation, we obtain

$$\Omega = \sqrt{\sum_l \Omega_l^2},$$

where

$$\begin{aligned} \Omega_l &= \frac{\Omega_X \sqrt{\hbar\omega_{\vec{q}} \lambda_X}}{\sqrt{E_{1s}}} \left[S_{\text{uc}}^{-1} \int_{\text{uc}} d\vec{\rho} \sum_{\alpha} |u_{\alpha, \vec{q}}(\vec{\rho}, z_l)|^2 \Theta(\vec{\rho}, z_l) \right]^{\frac{1}{2}} \\ &= \frac{d |\phi_1(0)| \sqrt{\omega_0}}{\sqrt{2\hbar\epsilon_0}} \left[S_{\text{uc}}^{-1} \int_{\text{uc}} d\vec{\rho} \sum_{\alpha} |u_{\alpha, \vec{Q}^{(v)}}(\vec{\rho}, z_l)|^2 \right]^{\frac{1}{2}}. \end{aligned}$$

In the final step, we have ignored the \vec{q} dependence of Ω in the vicinity of the energy minima at $\vec{Q}^{(v)}$ ($v = x, y$) and we have used the fact that all QWs are embedded in the solid central slab.

When exciton inhomogeneous broadening is considered, the exciton energy in the l th QW also contains a fluctuating part δE_l , i.e., $E_{1s}^{(l)}(\vec{q}) = E_{1s}(\vec{q}) + \delta E_l$. The Hamiltonian matrix

is then

$$\begin{pmatrix} \hbar\omega_{\vec{q}} & -i\hbar\Omega_1 & \cdots & -i\hbar\Omega_{N-1} & -i\hbar\Omega_N \\ i\hbar\Omega_1 & E_{1s}^{(1)}(\vec{q}) & \cdots & 0 & 0 \\ \vdots & 0 & \ddots & \vdots & \vdots \\ i\hbar\Omega_{N-1} & 0 & \cdots & E_{1s}^{(N-1)}(\vec{q}) & 0 \\ i\hbar\Omega_N & 0 & \cdots & 0 & E_{1s}^{(N)}(\vec{q}) \end{pmatrix} \quad (\text{C26})$$

with N being the number of QWs. The eigenvalues E and eigenvectors $\{v\}$ of the Hamiltonian matrix satisfy the following equations:

$$\sum_l \frac{\hbar^2 \Omega_l^2}{(E - \hbar\omega_{\vec{q}})[E - E_{1s}^{(l)}(\vec{q})]} = 1, \quad v_l = \frac{\hbar\Omega_l v_0}{E - E_{1s}^{(l)}(\vec{q})} \quad (\text{C27})$$

for $l = 1, \dots, N$ with

$$v_0 = \left[1 + \sum_l \frac{\hbar^2 \Omega_l^2}{[E_{\text{pol}} - E_{1s}^{(l)}(\vec{q})]^2} \right]^{-\frac{1}{2}}. \quad (\text{C28})$$

Hence the excitonic fraction of a polariton in the l th QW is

$$P_l = v_l^2 = \frac{\hbar^2 \Omega_l^2}{[E - E_{1s}^{(l)}(\vec{q})]^2} \left[1 + \sum_l \frac{\hbar^2 \Omega_l^2}{[E - E_{1s}^{(l)}(\vec{q})]^2} \right]^{-1}. \quad (\text{C29})$$

When there are QWs placed in the photonic-crystal cladding, such as in Refs. [28,36], the excitonic fraction varies significantly with the position of the QW. This is caused by the variation in overlap of the photonic field and the excitonic one. However, in the current work, since there are QWs only in the central slab, the overlap between the excitonic and photonic fields is nearly the same for all quantum wells, with $P_l = \frac{1}{3} P_x$ where $P_x = \sum_l P_l$, in the case of three quantum wells in the central slab. The photonic fraction is

$$P_0 = v_0^2 = \left[1 + \sum_l \frac{\hbar^2 \Omega_l^2}{[E - E_{1s}^{(l)}(\vec{q})]^2} \right]^{-1}. \quad (\text{C30})$$

Note that the eigenvalue equation (C27) can also be written as

$$\sum_{l,\alpha,n} \frac{\hbar^2 \overline{\Omega}_{l,\alpha,n,\vec{q}}^2}{(E - \hbar\omega_{\vec{q}})[E - E_{1s}^{(l)}(\vec{q} + \vec{G}_n)]} = 1, \quad (\text{C31})$$

which is Eq. (10) in the main text. The spectra of the upper and lower polariton branches are obtained by diagonalizing the system Hamiltonian numerically. From numerical diagonalization the two polariton branches are identified as the two modes which have the largest photonic fraction.

APPENDIX D: FIELD INTENSITY DISTRIBUTIONS IN VARIOUS ARCHITECTURES

We study the photonic field intensity distributions in the different architectures considered in Sec. V and how they affect the exciton-photon couplings. We assume the excitonic field is distributed uniformly in the semiconductor region. In each

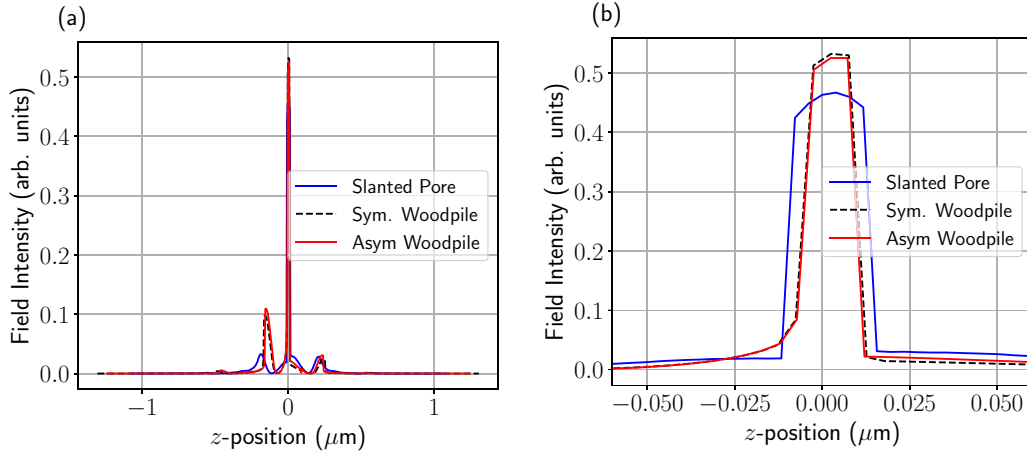


FIG. 17. (a) Field intensity distribution $S^{-1} \int d\vec{\rho} |\vec{\mathcal{E}}(\vec{\rho}, z)|^2$ along the growth axis in the slanted-pore and symmetric and asymmetric woodpile systems for band edge photons (at $\vec{Q}^{(y)}$ in the slanted-pore system and $\vec{Q}^{(x)}$ in the asymmetric and symmetric woodpile systems). To ensure $\Delta_{\vec{Q}^{(y)}} = 40$ meV, the lattice constant is $a = 240$ nm in the slanted-pore system, while $a = 270$ nm and $a = 275$ nm in the symmetric and asymmetric woodpile systems. (b) Same plot as (a), zoomed in on the region of the central slab.

of these photonic-crystal systems, we consider four unit cells of photonic crystal, composed of AlGaAs above and below a central slab layer containing the GaAs/AlGaAs MQWs. In the case of the slanted-pore system, the width of the central slab is $0.08a$ and in the case of the woodpile-based systems, the width of the central slab is $0.07a$. As described in Fig. 13, the lattice constant is about $a \approx 240$ nm and $a \approx 270$ nm in the slanted-pore and woodpile-based systems, respectively. These choices set the exciton-photon detuning $\Delta_{\vec{Q}^{(y)}} \approx 40$ meV. In Fig. 17(a), we plot the field intensity distributions along the growth axis for the slanted-pore and asymmetric and symmetric woodpile systems. Figure 17(b) is a magnified section of Fig. 17(a), depicting the region around the central slab. These results reveal that in the slanted-pore system, the peak field intensity is weaker than in the woodpile systems, but extends over a larger range in z . In the slanted-pore system, the interplay between this weaker field intensity (which diminishes $\hbar\Omega_{\vec{Q}^{(y)}}$) and the smaller lattice constant (which enhances $\hbar\Omega_{\vec{Q}^{(y)}}$ [cf. Eq. (9) and associated description]) ultimately results in very slightly weaker coupling strengths compared to the symmetric-woodpile system.

APPENDIX E: HIGH-MOMENTUM CUTOFF IN THE CALCULATION OF T_c

In computing the critical temperature in Eq. (16), we demand that the combined occupancy of the ground and excited states be equal to the total number of particles in the system. In this appendix, we elucidate the convergence of this process based on the number of excited states that are considered. That is to say, we show how the sum is truncated, based on both physical and numerical considerations.

For excitons having Bohr radius a_B trapped in a box trap of side length D , a simple physical argument provides an order-of-magnitude estimate of the number of permitted states of our system. We count only distinct exciton states, meaning that there is negligible spatial overlap between adjacent excitons. Approximating the spatial extent of the exciton wave functions as squares of area a_B^2 , an order-of-magnitude estimate of the

number of distinct exciton states in a 2D box of side length D is M^2 where $M \sim D/a_B$. The total number of distinct exciton states is the same in coordinate and momentum space. In momentum space, the box trap induces a discretization of the exciton-polariton wave vectors in increments of π/D in both the q_x and q_y directions. Subsequently, we consider momenta only up to $M\pi/D$ in both q_x and q_y . This is indicated in Fig. 4. For momenta higher than $q_{\text{cut}} \sim M\pi/D = \pi/a_B$, the de Broglie wavelength of the excitons would become smaller than the dimensions of the exciton and would probe the internal structure of the exciton itself.

We plot the critical temperature dependence on the actual numerical high-momentum cutoff in Fig. 18. The rapid convergence for $q_{\text{cut}} > \pi/a_B$ is consistent with the physical argument given above. Our results suggest that beyond a cutoff of $q_{\text{cut}} = 2\pi/a_B$ (for realistic values of the exciton-photon detuning, exciton-photon coupling strength, box trap side length, and exciton-polariton density), the critical temperature remains unchanged. Therefore, we take $q_{\text{cut}} = 2\pi/a_B$ for all of our calculations. The large critical temperature for very small momentum cutoffs is an artifact of ignoring the large number of excitonlike states and placing too much statistical weight on the low-energy photonlike states.

APPENDIX F: EFFECT OF HIGHER EXCITONIC STATES AND OTHER CONFINED PHOTONIC BANDS

1. A method for multiple-mode coupling

To discuss the effect of higher excitonic states and other confined photonic bands on the polariton spectrum, we present a method to simplify the diagonalization of a large matrix. The general form of the exciton-photon coupling Hamiltonian is

$$H = \sum_i \hbar\omega_i a_i^\dagger a_i + \sum_j E_j b_j^\dagger b_j + \sum_{i,j} (g_{i,j} a_i^\dagger b_j + g_{i,j}^* b_j^\dagger a_i) \quad (\text{F1})$$

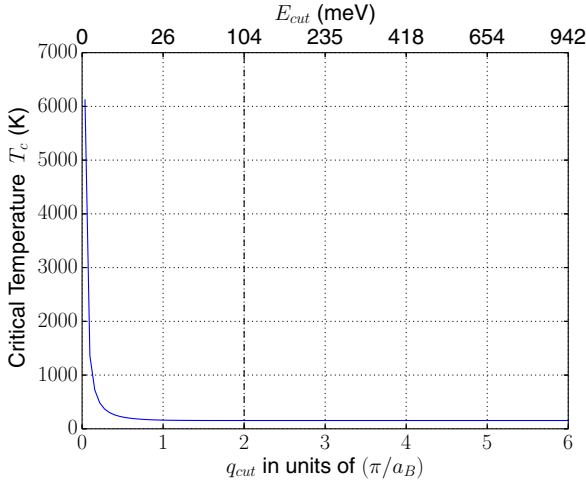


FIG. 18. The critical temperature computed from Eq. (16) as a function of the high-momentum cutoff q_{cut} . Here, the exciton-photon detuning is $\Delta_{\vec{Q}(x)} = \Delta_{\vec{Q}(y)} = 30$ meV, the exciton-photon coupling is $\hbar\Omega_{\vec{Q}(x)} = \hbar\Omega_{\vec{Q}(y)} = 15$ meV, the box-trap side length is $D = 10\mu\text{m}$, and the polariton density is $(5a_B)^{-2}$ where $a_B = 9$ nm is the exciton Bohr radius. The exciton mass is $m_{\text{exc}} = 0.176m_0$, the photon effective mass is $m_{\text{ph}} = 5 \times 10^{-6}m_0$, and the condensate fraction is $f = 0.1$. The dashed line indicates the momentum cutoff at $q_{\text{cut}} = 2\pi/a_B$, which we use throughout the paper. The upper horizontal axis indicates by how much, in energy, the bare exciton has dispersed at the corresponding q_{cut} .

with $i = 1, \dots, N_1$ and $j = 1, \dots, N_2$ labeling the states of photon and exciton, respectively. We are interested in the lowest eigenvalue E_{LP} and its eigenstate φ of the Hamiltonian which correspond to the lower polariton branch. That is

$$\begin{pmatrix} \hat{H}_1 & \hat{S} \\ \hat{S}^\dagger & \hat{H}_2 \end{pmatrix} \begin{pmatrix} \varphi_1 \\ \varphi_2 \end{pmatrix} = E_{\text{LP}} \begin{pmatrix} \varphi_1 \\ \varphi_2 \end{pmatrix}, \quad (\text{F2})$$

where \hat{H}_1 (\hat{H}_2) is the Hamiltonian of photon (exciton), \hat{S} is their mutual coupling, and φ_1 (φ_2) is the eigenfunction in the photon (exciton) sector. Eliminating φ_2 from Eq. (F2) yields

$$\hat{H}^{\text{eff}} \varphi_1 = E_{\text{LP}} \varphi_1, \quad (\text{F3a})$$

$$\hat{H}^{\text{eff}} = \hat{H}_1 + \hat{S}(E_{\text{LP}}\hat{1} - \hat{H}_2)^{-1}\hat{S}^\dagger. \quad (\text{F3b})$$

It is easier to solve the problem in the photon sector because $N_1 \ll N_2$. Numerically, the calculation is done by a recursive method. To implement this method, we begin with an estimate of E_{LP} which can be obtained from Eq. (10). Using this value of E_{LP} , we construct the Hamiltonian \hat{H}^{eff} , diagonalize it, and take the lowest eigenvalue, \tilde{E}_{LP} . We then use \tilde{E}_{LP} as the new E_{LP} and use it to construct \hat{H}^{eff} again. We repeat this process iteratively. After sufficient iteration, E_{LP} can be found to the desired precision. In this work, we iterate this process approximately 10^3 times until the fractional difference in eigenvalues $\frac{\tilde{E}_{\text{LP}} - E_{\text{LP}}}{E_{\text{LP}}}$ falls below 10^{-6} . After having found E_{LP} to the desired precision, one can then obtain the eigenstate φ_1 . Then, through

$$\varphi_2 = (E_{\text{LP}}\hat{1} - \hat{H}_2)^{-1}\hat{S}^\dagger\varphi_1, \quad (\text{F4})$$

we can obtain the eigenstate φ_2 in the exciton sector. The specific form of \hat{H}^{eff} is rather simple:

$$H_{i_1, i_2}^{\text{eff}} = \hbar\omega_{i_1} \delta_{i_1, i_2} + \sum_j S_{i_1, j} (E_{\text{LP}} - E_j)^{-1} S_{i_2, j}^*. \quad (\text{F5})$$

We now describe the calculation of the second term (referred to as the self-energy) in Eq. (F5). This is essentially second-order Brillouin-Wigner perturbation theory, which is equivalent to solving the problem in restricted variational subspace with a single polariton.

We consider excitons in the p th s orbital in a single quantum well. The exciton-photon coupling term is written as [cf. Eq. (8d)]

$$H_{\text{int}} = \sum_{\alpha, p, n, i, \vec{q}} i \hbar \bar{\Omega}_{\alpha, p, n, i, \vec{q}} \beta_{\alpha, p, \vec{q} + \vec{G}_n}^\dagger a_{i, \vec{q}} + \text{H.c.} \quad (\text{F6})$$

The self-energy is then

$$\Sigma_{i_1, i_2}(\vec{q}) = \sum_{\alpha, p, n} \frac{\hbar^2 \bar{\Omega}_{\alpha, p, n, i_1, \vec{q}}^* \bar{\Omega}_{\alpha, p, n, i_2, \vec{q}}}{E_{\text{LP}} - E_{\alpha, n}(\vec{q})}. \quad (\text{F7})$$

Inserting the specific expression for the exciton-photon coupling,

$$\hbar \bar{\Omega}_{\alpha, n, i, \vec{q}} = d\phi_1(0) u_{\alpha, i, \vec{q}, \vec{G}_n}(z_0) \sqrt{\hbar\omega_{\vec{q}}/2\epsilon_0}, \quad (\text{F8})$$

into Eq. (F7) and using $E_{\alpha, n}(\vec{q}) \simeq E(\vec{q})$ (meaning that the inhomogeneous broadening of the exciton between different

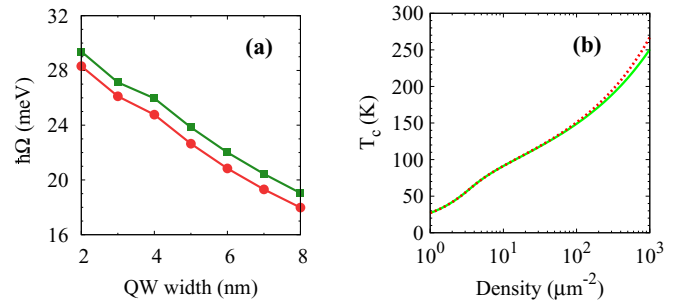


FIG. 19. (a) Collective exciton-photon coupling in the symmetric woodpile of Fig. 1(a) with (curve with squares) and without (curve with dots) the contribution from the higher excitonic and photonic states. The parameters are the same as in Fig. 9(a), with the exception that approximately 110 QWs populate both the central slab layer and the first unit cell of symmetric woodpile above and below the central slab. (b) Transition temperature as a function of the polariton density for two scenarios. For one scenario (solid green curve) higher photonic bands are ignored. For the other scenario (dotted red curve) four degenerate higher photonic bands are considered. The band edge is 80 meV higher than that of the lowest confined photonic band and the effective mass is 1000 times as large as that of the lowest confined photonic band. The coupling constant $\hbar\Omega_{\vec{Q}(x)} = 28$ meV, and the exciton recombination energy is 1.966 eV. The box side length is $D = 10\mu\text{m}$ and the lattice constant of the symmetric woodpile is $a = 269$ nm.

QWs is small), we obtain

$$\Sigma_{i_1, i_2}(\vec{q}) = \frac{d^2 \hbar \sqrt{\omega_{i_1} \omega_{i_2}}}{2\varepsilon_0} \sum_p \frac{\phi_p^2(0)}{[E_{LP} - E_{ps}(\vec{q})]} S_{uc}^{-1} \times \sum_{\alpha} \int_{uc} d\vec{\rho} u_{\alpha, i_1}^*(\vec{\rho}, z_0) u_{\alpha, i_2}(\vec{\rho}, z_0), \quad (F9)$$

where $E_{ps}(\vec{q})$ is the energy of the exciton in the p th s orbital with wave vector \vec{q} . The summation over all s -orbital exciton states converges very quickly as the amplitude $\phi_p^2(0)$ decreases rapidly with the index p . In the limit that we consider only 1s excitons, Eq. (F9) becomes

$$\begin{aligned} \Sigma_{i_1, i_2}(\vec{q}) &= \sum_{\alpha, n} \frac{\hbar^2 \bar{\Omega}_{\alpha, n, i_1, \vec{q}}^* \bar{\Omega}_{\alpha, n, i_2, \vec{q}}}{E_{LP} - E_{1s}(\vec{q})} \\ &= \frac{\phi_1^2(0) d^2 \hbar \sqrt{\omega_{i_1} \omega_{i_2}}}{2\varepsilon_0 [E_{LP} - E_{1s}(\vec{q})]} \sum_{\alpha, n} u_{\alpha, i_1, \vec{q}, \vec{G}_n}(z_0)^* u_{\alpha, i_2, \vec{q}, \vec{G}_n}(z_0) \\ &= \frac{\phi_1^2(0) d^2 \hbar \sqrt{\omega_{i_1} \omega_{i_2}}}{2\varepsilon_0 [E_{LP} - E_{1s}(\vec{q})]} S_{uc}^{-1} \\ &\times \sum_{\alpha} \int_{uc} d\vec{\rho} u_{\alpha, i_1}^*(\vec{\rho}, z_0) u_{\alpha, i_2}(\vec{\rho}, z_0). \end{aligned} \quad (F10)$$

For the structure with MQWs we need to sum over the contribution from each QW. The contribution from the l th QW in the slab layer is

$$\sum_{\alpha} \int_{uc} d\vec{\rho} u_{\alpha, i_1}^*(\vec{\rho}, z_l) u_{\alpha, i_2}(\vec{\rho}, z_l). \quad (F11)$$

Therefore the whole expression for the self-energy is

$$\begin{aligned} \Sigma_{i_1, i_2}(\vec{q}) &= \frac{d^2 \hbar \sqrt{\omega_{i_1} \omega_{i_2}}}{2\varepsilon_0} \sum_p \frac{\phi_p^2(0)}{[E_{LP} - E_{ps}(\vec{q})]} S_{uc}^{-1} \\ &\times \sum_{l, \alpha} \int_{uc} d\vec{\rho} u_{\alpha, i_1}^*(\vec{\rho}, z_l) u_{\alpha, i_2}(\vec{\rho}, z_l). \end{aligned} \quad (F12)$$

2. Numerical results

We find that including higher excitonic states and other confined photonic bands modifies the collective exciton-photon coupling only slightly and can safely be ignored. The results, calculated using the method of the previous section, are plotted in Fig. 19(a).

We show that higher confined photonic bands do not affect the transition temperature given the predominance of the huge excitonic density of states. In Fig. 19(b) we plot the transition temperature of polariton BEC as a function of density for two cases, one without higher photonic bands (the solid curve) and the other case with the four lowest photonic bands. The edge of the second lowest band is 80 meV above the edge of the lowest confined photonic band. The effective mass of higher bands is roughly 1000 times that of the lowest confined photonic band. Clearly, high density of states of other low-lying photonic bands is overwhelmed by the even higher excitonic density of states and the BEC transition temperature is barely affected.

-
- [1] A. Einstein, Quantentheorie des einatomigen idealen Gases [Quantum theory of ideal monoatomic gases], Sitz. Ber. Preuss. Akad. Wiss. **23**, 3 (1925).
- [2] F. London, The λ -phenomenon of liquid Helium and the Bose-Einstein degeneracy, *Nature (London)* **141**, 643 (1938); On the Bose-Einstein condensation, *Phys. Rev.* **54**, 947 (1938).
- [3] O. Penrose and L. Onsager, Bose-Einstein condensation and liquid Helium, *Phys. Rev.* **104**, 576 (1956).
- [4] H. K. Onnes, The resistance of pure mercury at helium temperatures, *Commun. Phys. Lab. Univ. Leiden* **12**, 120 (1911).
- [5] J. Bardeen, L. N. Cooper, and J. R. Schrieffer, Theory of superconductivity, *Phys. Rev.* **108**, 1175 (1957).
- [6] M. H. Anderson, J. R. Ensher, M. R. Matthews, C. E. Wieman, and E. A. Cornell, Observation of Bose-Einstein condensation in a dilute atomic vapor, *Science* **269**, 198 (1995).
- [7] K. B. Davis, M.-O. Mewes, M. R. Andrews, N. J. van Druten, D. S. Durfee, D. M. Kurn, and W. Ketterle, Bose-Einstein Condensation in a Gas of Sodium Atoms, *Phys. Rev. Lett.* **75**, 3969 (1995).
- [8] H. Deng, G. Weihs, C. Santori, J. Bloch, and Y. Yamamoto, Condensation of semiconductor microcavity exciton polaritons, *Science* **298**, 199 (2002).
- [9] H. Deng, G. Weihs, D. Snoke, J. Bloch, and Y. Yamamoto, Polariton lasing vs. photon lasing in a semiconductor microcavity, *Proc. Natl. Acad. Sci. USA* **100**, 15318 (2003).
- [10] M. Richard, J. Kasprzak, R. Romestain, R. André, and L. S. Dang, Spontaneous Coherent Phase Transition of Polaritons in CdTe Microcavities, *Phys. Rev. Lett.* **94**, 187401 (2005).
- [11] J. Kasprzak, M. Richard, S. Kundermann, A. Baas, P. Jeambrun, J. M. J. Keeling, F. M. Marchetti, M. H. Szymaska, R. André, J. L. Staehli, V. Savona, P. B. Littlewood, B. Deveaud, and L. S. Dang, Bose-Einstein condensation of exciton polaritons, *Nature (London)* **443**, 409 (2006).
- [12] R. Balili, V. Hartwell, D. Snoke, L. Pfeiffer, and K. West, Bose-Einstein condensation of microcavity polaritons in a trap, *Science* **316**, 1007 (2007).
- [13] H. Deng, H. Haug, and Y. Yamamoto, Exciton-polariton Bose-Einstein condensation, *Rev. Mod. Phys.* **82**, 1489 (2010).
- [14] D. G. Lidzey, D. D. C. Bradley, T. Virgili, A. Armitage, M. S. Skolnick, and S. Walker, Room Temperature Polariton Emission from Strongly Coupled Organic Semiconductor Microcavities, *Phys. Rev. Lett.* **82**, 3316 (1999); S. Christopoulos, G. Baldassarri, H. von Högersthal, A. J. D. Grundy, P. G. Lagoudakis, A. V. Kavokin, J. J. Baumberg, G. Christmann, R. Butté, E. Feltn, J.-F. Carlin, and N. Grandjean, Room-Temperature Polariton Lasing in Semiconductor Microcavities, *ibid.* **98**, 126405 (2007); G. Christmann, R. Butté, E. Feltn, J.-F. Carlin, and N. Grandjean, Room temperature polariton lasing in a GaN/AlGaIn multiple quantum well microcavity, *Appl. Phys. Lett.* **93**, 051102 (2008); S. Kéna-Cohen and S. R. Forrest,

- Room-temperature polariton lasing in an organic single-crystal microcavity, *Nat. Photon.* **4**, 371 (2010); Y.-Y. Lai, Y.-P. Lan, and T.-C. Lu, Strong light-matter interaction in ZnO microcavities, *Light: Sci. Applic.* **2**, e76 (2013).
- [15] C. Weisbuch, M. Nishioka, A. Ishikawa, and Y. Arakawa, Observation of the Coupled Exciton-Photon Mode Splitting in a Semiconductor Quantum Microcavity, *Phys. Rev. Lett.* **69**, 3314 (1992).
- [16] D. Sanvitto, F. M. Marchetti, M. H. Szymańska, G. Tosi, M. Baudisch, F. P. Laussy, D. N. Krizhanovskii, M. S. Skolnick, L. Marrucci, A. Lemaître, J. Bloch, C. Tejedor, and L. Viña, Persistent currents and quantized vortices in a polariton superfluid, *Nat. Phys.* **6**, 527 (2010).
- [17] K. G. Lagoudakis, M. Wouters, M. Richard, A. Baas, I. Carusotto, R. André, L. S. Dang, and B. Deveaud-Plédran, Quantized vortices in an exciton-polariton condensate, *Nat. Phys.* **4**, 706 (2008).
- [18] See, e.g., D. Ballarini, D. Sanvitto, A. Amo, L. Viña, M. Wouters, I. Carusotto, A. Lemaitre, and J. Bloch, Observation of Long-Lived Polariton States in Semiconductor Microcavities Across the Parametric Threshold, *Phys. Rev. Lett.* **102**, 056402 (2009).
- [19] B. Nelsen, G. Liu, M. Steger, D. W. Snoke, R. Balili, K. West, and L. Pfeiffer, Dissipationless Flow and Sharp Threshold of a Polariton Condensate with Long Lifetime, *Phys. Rev. X* **3**, 041015 (2013).
- [20] I. Carusotto and C. Ciuti, Quantum fluids of light, *Rev. Mod. Phys.* **85**, 299 (2013).
- [21] K. G. Lagoudakis, T. Ostatnický, A. V. Kavokin, Y. G. Rubo, R. André, and B. Deveaud-Plédran, Observation of half-quantum vortices in an exciton-polariton condensate, *Science* **326**, 974 (2009).
- [22] See, e.g., A. Aspuru-Guzik and P. Wlther, Photonic quantum simulators, *Nat. Phys.* **8**, 285 (2012).
- [23] C. Schneider, A. Rahimi-Iman, N. Y. Kim, J. Fischer, I. G. Savenko, M. Amthor, M. Lermer, A. Wolf, L. Worschech, V. D. Kulakovskii, I. A. Shelykh, M. Kamp, S. Reitzenstein, A. Forchel, Y. Yamamoto, and S. Höfling, An electrically pumped polariton laser, *Nature (London)* **497**, 348 (2013).
- [24] A. Amo, T. C. H. Liew, C. Adrados, R. Houdré, E. Giacobino, A. V. Kavokin, and A. Bramati, Exciton-polariton spin switches, *Nat. Photon.* **4**, 361 (2010).
- [25] D. Ballarini, M. De Giorgi, E. Cancellieri, R. Houdré, E. Giacobino, R. Cingolani, A. Bramati, G. Gigli, and D. Sanvitto, All-optical polariton transistor, *Nat. Commun.* **4**, 1778 (2013).
- [26] Y. Sun, P. Wen, Y. Yoon, G. Liu, M. Steger, L. N. Pfeiffer, K. West, D. W. Snoke, and K. A. Nelson, Bose-Einstein Condensation of Long-Lifetime Polaritons in Thermal Equilibrium, *Phys. Rev. Lett.* **118**, 016602 (2017).
- [27] L. V. Butov and A. V. Kavokin, The behaviour of exciton-polaritons, *Nat. Photon.* **6**, 2 (2012); B. Deveaud-Plédran, The behaviour of exciton-polaritons, *ibid.* **6**, 205 (2012).
- [28] J.-H. Jiang and S. John, Photonic Crystal Architecture for Room-Temperature Equilibrium Bose-Einstein Condensation of Exciton Polaritons, *Phys. Rev. X* **4**, 031025 (2014).
- [29] P. Vasudev, J.-H. Jiang, and S. John, Light-trapping for room temperature Bose-Einstein condensation in InGaAs quantum wells, *Opt. Express* **24**, 14010 (2016).
- [30] J. D. Joannopoulos, S. G. Johnson, J. N. Winn, and R. D. Meade, *Photonic Crystals: Molding the Flow of Light*, 2nd ed. (Princeton University Press, Princeton, 2008).
- [31] S. John and S. J. Yang, Electromagnetically Induced Exciton Mobility in a Photonic Band Gap, *Phys. Rev. Lett.* **99**, 046801 (2007).
- [32] S. J. Yang and S. John, Exciton dressing and capture by a photonic band edge, *Phys. Rev. B* **75**, 235332 (2007).
- [33] S. J. Yang and S. John, Coherence and antibunching in a trapped interacting Bose-Einstein condensate, *Phys. Rev. B* **84**, 024515 (2011).
- [34] D. Caputo, D. Ballarini, G. Dagvadorj, C. S. Muñoz, M. De Giorgi, L. Dominici, K. West, L. N. Pfeiffer, G. Gige, F. P. Laussy, M. H. Szymańska, and D. Sanvitto, Topological order and equilibrium in a condensate of exciton-polaritons, [arXiv:1610.05737](https://arxiv.org/abs/1610.05737).
- [35] G. Roumpos, M. Lohse, W. H. Nitsche, J. Keeling, M. H. Szymańska, P. B. Littlewood, A. Löffler, S. Höfling, L. Worschech, A. Forchel, and Y. Yamamoto, Power-law decay of the spatial correlation function in exciton-polariton condensates, *Proc. Natl. Acad. Sci. USA* **109**, 6467 (2012).
- [36] J.-H. Jiang and S. John, Photonic architectures for equilibrium high-temperature Bose-Einstein condensation in dichalcogenide monolayers, *Sci. Rep.* **4**, 7432 (2014).
- [37] Y. Takahashi, H. Hagino, Y. Tanaka, B.-S. Song, T. Asano, and S. Noda, High-Q nanocavity with a 2-ns photon lifetime, *Opt. Express* **15**, 17206 (2007).
- [38] S. John, Electromagnetic Absorption in a Disordered Medium near a Photon Mobility Edge, *Phys. Rev. Lett.* **53**, 2169 (1984); Strong Localization of Photons in Certain Disordered Dielectric Superlattices, **58**, 2486 (1987); E. Yablonovitch, Inhibited Spontaneous Emission in Solid-State Physics and Electronics, *ibid.* **58**, 2059 (1987); S. John and J. Wang, Quantum Electrodynamics Near a Photonic Band Gap: Photon Bound States and Dressed Atoms, *ibid.* **64**, 2418 (1990).
- [39] S. Oertel, J. Hübner, and M. Oestreich, High temperature electron spin relaxation in bulk GaAs, *Appl. Phys. Lett.* **93**, 132112 (2008).
- [40] A. V. Gopal, R. Kumar, A. S. Vengurlekar, A. Bosacchi, S. Franchi, and L. N. Pfeiffer, Photoluminescence study of exciton-optical phonon scattering in bulk GaAs and GaAs quantum wells, *Appl. Phys. Lett.* **87**, 1858 (2000).
- [41] S. Ogawa, M. Imada, S. Yoshimoto, M. Okano, and S. Noda, Control of light emission by 3D photonic crystals, *Science* **305**, 227 (2004).
- [42] S. Noda, M. Fujita, and T. Asano, Spontaneous-emission control by photonic crystals and nanocavities, *Nat. Photon.* **1**, 449 (2007).
- [43] N. Téterault, V. von Freymann, M. Deubel, M. Hermatschweiler, F. Prez-Willard, S. John, M. Wegener, and G. A. Ozin, New route to three-dimensional photonic bandgap materials: Silicon double inversion of polymer templates, *Adv. Mater.* **18**, 457 (2006).
- [44] S. Juodkakis, L. Rosa, S. Bauerdick, L. Peto, R. El-Ganainy, and S. John, Sculpturing of photonic crystals by ion beam lithography: Towards complete photonic bandgap at visible wavelengths, *Opt. Express* **19**, 5802 (2011).
- [45] M. Deubel, M. Wegener, A. Kaso, and S. John, Direct laser writing and characterization of slanted pore photonic crystals, *Appl. Phys. Lett.* **85**, 1895 (2004).
- [46] We use the MIT Photonic-Bands package to do the calculation. See http://ab-initio.mit.edu/wiki/index.php/MIT_Phonic_Bands.

- [47] Calculations via the finite difference time domain method are also performed for some cases. We also compared the calculations from both the plane wave expansion method and the finite difference time domain method and find that the difference between the two is very small.
- [48] P. Harrison, *Quantum Wells, Wires and Dots* (Wiley, New York, 2001).
- [49] R. Winkler, *Spin-Orbit Coupling Effects in Two-Dimensional Electron and Hole Systems* (Springer, Berlin, 2003), Chap. 4.5.
- [50] O. Madelung, *Semiconductors: Data Handbook*, 3rd ed. (Springer, Berlin, 2004).
- [51] I. Vurgaftman, J. R. Meyer, and L. R. Ram-Mohan, Band parameters for III-V compound semiconductors and their alloys, *J. Appl. Phys.* **89**, 5815 (2001).
- [52] M. S. Dresselhaus, G. Dresselhaus, and A. Jorio, *Applications of Group Theory to the Physics of Solids*, 1st ed. (Springer, Berlin, 2008).
- [53] D. A. Broido and L. J. Sham, Valence-band coupling and Fano-resonance effects on the excitonic spectrum in undoped quantum wells, *Phys. Rev. B* **34**, 3917 (1986).
- [54] J. M. Luttinger, *Phys. Rev.* **102**, 1030 (1956).
- [55] Y. Yamamoto, F. Tassone, and H. Cao, *Semiconductor Cavity Quantum Electrodynamics*, 1st ed. (Springer, Berlin, 2000).
- [56] L. C. Andreani and F. Bassani, Exchange interaction and polariton effects in quantum-well excitons, *Phys. Rev. B* **41**, 7536 (1990).
- [57] H. Tong and M. W. Wu, Theory of excitons in cubic III-V semiconductor GaAs, InAs, and GaN quantum dots: Fine structure and spin relaxation, *Phys. Rev. B* **83**, 235323 (2011).
- [58] W. Ketterle and N. J. van Druten, Bose-Einstein condensation of a finite number of particles trapped in one or three dimensions, *Phys. Rev. A* **54**, 656 (1996).
- [59] E. J. Mueller, T.-L. Ho, M. Ueda, and G. Baym, Fragmentation of Bose-Einstein condensates, *Phys. Rev. A* **74**, 033612 (2006).
- [60] See <http://ab-initio.mit.edu/wiki/index.php/Meep>.
- [61] O. Toader, M. Berciu, and S. John, Photonic Band Gaps Based on Tetragonal Lattices of Slanted Pores, *Phys. Rev. Lett.* **90**, 233901 (2003); O. Toader and S. John, Slanted-pore photonic band-gap materials, *Phys. Rev. E* **71**, 036605 (2005).
- [62] S. Schmitt-Rink, D. S. Chemla, and D. A. B. Miller, Theory of transient excitonic optical nonlinearities in semiconductor quantum-well structures, *Phys. Rev. B* **32**, 6601 (1985).
- [63] A. Honold, L. Schultheis, J. Kuhl, and C. W. Tu, Collision broadening of two-dimensional excitons in a GaAs single quantum well, *Phys. Rev. B* **40**, 6442 (1989).
- [64] S. I. Tsintzos, P. G. Savvidis, G. Deligeorgis, Z. Hatzopoulos, and N. T. Pelekanos, Room temperature GaAs exciton-polariton light emitting diode, *Appl. Phys. Lett.* **94**, 071109 (2009).
- [65] M. Govoni, I. Marri, and S. Ossicini, Auger recombination in Si and GaAs semiconductors: Ab initio results, *Phys. Rev. B* **84**, 075215 (2011).
- [66] W. Shockley and W. T. Read, Jr., Statistics of the recombinations of holes and electrons, *Phys. Rev.* **87**, 835 (1952); R. N. Hall, Electron-Hole recombination in germanium, *ibid.* **87**, 387 (1951).
- [67] E. Nelson, N. L. Dias, K. P. Bassett, S. N. Dunham, V. Verma, M. Miyake, P. Wiltzius, J. A. Rogers, J. J. Coleman, X. Li, and P. V. Braun, Epitaxial growth of three-dimensionally architected optoelectronic devices, *Nat. Mater.* **10**, 676 (2011).
- [68] D. E. Aspnes and A. A. Studna, Dielectric functions and optical parameters of Si, Ge, GaP, GaAs, GaSb, InP, InAs, and InSb from 1.5 to 6.0 eV, *Phys. Rev. B* **27**, 985 (1983).
- [69] *The Physics of Semiconductor Microcavities*, edited by B. Deveaud (Wiley-VCH, Weinheim, 2007).
- [70] V. Savona, L. C. Andreani, P. Schwendimann, and A. Quattropani, Quantum well excitons in semiconductor microcavities: Unified treatment of weak and strong coupling regimes, *Solid State Commun.* **93**, 733 (1995).
- [71] G. Khitrova, H. M. Gibbs, M. Kira, S. W. Koch, and A. Scherer, Vacuum Rabi splitting in semiconductors, *Nat. Phys.* **2**, 81 (2006).
- [72] F. Dalfovo, S. Giorgini, L. P. Pitaevskii, and S. Stringari, Theory of Bose-Einstein condensation in trapped gases, *Rev. Mod. Phys.* **71**, 463 (1999).
- [73] J. M. Kosterlitz and D. J. Thouless, Ordering, metastability and phase transitions in two-dimensional systems, *J. Phys. C* **6**, 1181 (1973).
- [74] A. Das, P. Bhattacharya, J. Heo, A. Banerjee, and W. Guo, Polariton Bose-Einstein condensate at room temperature in an Al(Ga)N nanowire-dielectric microcavity with a spatial potential trap, *Proc. Natl. Acad. Sci. USA* **110**, 2735 (2013).
- [75] I. V. Ponomarev, L. I. Deych, and A. A. Lisyansky, Interface disorder and inhomogeneous broadening of quantum well excitons: Do narrow lines always imply high-quality interfaces? *Appl. Phys. Lett.* **85**, 2496 (2004).
- [76] E. Hanamura and H. Haug, Condensation effects of excitons, *Phys. Rep.* **33**, 209 (1977).
- [77] Z. Holaman, A. Descoeudres, L. L. Arraud, F. Z. Fernandez, J. P. Seif, S. D. Wolf, and C. Ballif, Current losses at the front of silicon heterojunction solar cells, *IEEE J. Photovoltaics* **2**, 2156 (2012).
- [78] R. E. Treharne, A. Seymour-Pierce, K. Durose, K. Hutchings, S. Roncallo, and D. Lane, Optical design and fabrication of fully sputtered CdTe/CdS solar cells, *J. Phys.: Conf. Ser.* **286**, 012038 (2011).
- [79] G. D. Boyd, E. Buehler, F. G. Storz, and J. H. Wernick, Linear and nonlinear optical properties of ternary $A^{II}B^{IV}C_2^V$ chalcopyrite semiconductors, *IEEE J. Quantum Electron.* **8**, 419 (1972).
- [80] M. W. Wu, J. H. Jiang, and M. Q. Weng, Spin dynamics in semiconductors, *Phys. Rep.* **493**, 61 (2010).